DTU Library

Short-term variations of Icelandic ice cap mass inferred from cGPS coordinate time series

Compton, Kathleen; Bennett, Richard A.; Hreinsdóttir, Sigrún; van Dam, Tonie; Bordoni, Andrea; Barletta, Valentina Roberta; Spada, Giorgio

Link back to DTU Orbit

RESEARCH ARTICLE

Key Points:
- cGPS may be used as a low-cost ice mass balance measurement tool in Iceland
- cGPS-derived ice mass variation time series reproduce interannual variability in precipitation and melting
- Increased temporal resolution allows for better characterization of ice cap response following volcanic eruptions

Correspondence to:
K. Compton,
kcompton@email.arizona.edu

Short-term variations of Icelandic ice cap mass inferred from cGPS coordinate time series

Kathleen Compton[1] , Richard A. Bennett[1], Sigrún Hreinsdóttir[2,3] , Tonie van Dam[4] , Andrea Bordoni[5], Valentina Barletta[6], and Giorgio Spada[7]

[1]Department of Geosciences, University of Arizona, Tucson, Arizona, USA, [2]Institute of Earth Sciences, University of Iceland, Reykjavík, Iceland, [3]Now at GNS Science, Lower Hutt, New Zealand, [4]Faculté des Sciences, de la Technologie et de la Communication, University of Luxembourg, Luxembourg, Luxembourg, [5]DTU Compute, Technical University of Denmark, Lyngby, Denmark, [6]DTU Space, Technical University of Denmark, Lyngby, Denmark, [7]Dipartimento di Scienze Pure e Applicate, Università degli Studi di Urbino "Carlo Bo," Urbino, Italy

Abstract As the global climate changes, understanding short-term variations in water storage is increasingly important. Continuously operating Global Positioning System (cGPS) stations in Iceland record annual periodic motion—the elastic response to winter accumulation and spring melt seasons—with peak-to-peak vertical amplitudes over 20 mm for those sites in the Central Highlands. Here for the first time for Iceland, we demonstrate the utility of these cGPS-measured displacements for estimating seasonal and shorter-term ice cap mass changes. We calculate unit responses to each of the five largest ice caps in central Iceland at each of the 62 cGPS locations using an elastic half-space model and estimate ice mass variations from the cGPS time series using a simple least squares inversion scheme. We utilize all three components of motion, taking advantage of the seasonal motion recorded in the horizontal. We remove secular velocities and accelerations and explore the impact that seasonal motions due to atmospheric, hydrologic, and nontidal ocean loading have on our inversion results. Our results match available summer and winter mass balance measurements well, and we reproduce the seasonal stake-based observations of loading and melting within the 1σ confidence bounds of the inversion. We identify nonperiodic ice mass changes associated with interannual variability in precipitation and other processes such as increased melting due to reduced ice surface albedo or decreased melting due to ice cap insulation in response to tephra deposition following volcanic eruptions, processes that are not resolved with once or twice-yearly stake measurements.

1. Introduction

Iceland is home to some of the most climatically sensitive glaciers in the world [*Aðalgeirsdóttir et al.*, 2006; *Hock et al.*, 2009] and understanding their behavior in a changing climate is important for managing the country's largest freshwater reservoir. Ice cap height and extent derived from aerial photographs, Synthetic Aperture Radar (SAR) [e.g., *Magnússon et al.*, 2005; *Gudmundsson et al.*, 2011], and lidar [e.g., *Jóhannesson et al.*, 2013], which provide insight into changes over multiple years, field stake-based surface mass balance measurements, which identify total mass loss from year-to-year [e.g., *Björnsson et al.*, 2013], and Gravity Recovery and Climate Experiment (GRACE)-derived mass change estimates [e.g., *Wouters et al.*, 2008; *Jacob et al.*, 2012; *Sørensen et al.*, 2017], allow us to track how Icelandic ice caps have responded to climactic changes over multiyear and decadal time scales. Since the mid-1990s, Icelandic ice caps have been losing mass at a rate of 5.8–11.4 Gt/yr [*Wouters et al.*, 2008; *Jacob et al.*, 2012; *Björnsson et al.*, 2013; *Zhao et al.*, 2014; *Foresta et al.*, 2016; *Sørensen et al.*, 2017], a direct result of increasing summer temperatures.

It is also important to track ice cap mass changes on time scales of less than 1 year. Seasonal variations in winter snowfall and summer melting impact river discharge and water availability for utilities such as hydropower [e.g., *Jónsdóttir*, 2010]. However, current mass-balance methods suffer from coarse temporal resolution, and at present our toolbox to quantify short-term variability in ice cap mass is somewhat limited. For example, some stake mass balance measurements do provide a summer *and* winter balance, which can be used to constrain peak-to-peak seasonal changes, but are unable to capture variations on a monthly time scale. InSAR measurements can be used to infer the relationship between ice-loading histories and glacial

surges, Earth's properties, and surface displacements, but is often limited to near-field observations—in close proximity to the edge of an ice cap—and measurements are only possible in the summer due to interferogram decorrelation caused by seasonal snow cover in the winter [e.g., *Auriac et al.*, 2013, 2014; *Zhao et al.*, 2014]. GRACE data—provided that biasing by the much stronger signal from the nearby Greenland ice sheet is processed contextually and removed accordingly [*Sørensen et al.*, 2017]—can provide information about variations in surface mass over the whole of Iceland at a monthly time scale, However, GRACE-derived mass variations are currently limited to spatial resolutions of ∼300 km [*Tapley et al.*, 2004], which is too coarse for even the largest of the Icelandic ice caps. cGPS, alternatively, because of the dense Icelandic network, may provide information about the surface response to mass changes at a finer spatial scale and illuminate short-term changes on individual ice caps.

Studies using GPS have shed light on the impacts of glacial melt on the long-term crustal vertical velocity field in Iceland [e.g., *Árnadóttir et al.*, 2009; *Geirsson et al.*, 2010] as well was the annual periodic crustal motion due to seasonal loading and unloading [*Grapenthin et al.*, 2006; *Pinel et al.*, 2007], though to date, no study of Iceland has investigated the utility of cGPS-measured crustal motions to estimate a time series of mass variation. *Zhao et al.* [2014] demonstrated the efficacy of inverting bedrock uplift in Iceland to solve for mass loss on the Vatnajökull ice cap using InSAR observations, and have set the precedent that such an inversion can yield valuable information. However, *Zhao et al.* [2014] acknowledge that an inversion using InSAR suffers from several limiting factors, noting that InSAR measurements are much more sensitive to short-wavelength signals in close proximity to an ice cap edge and that all InSAR observations were collected from the east and southeast edge of the Vatnajökull ice cap. In contrast, the wide spatial distribution of cGPS stations in Iceland allows for investigation of both near and far-field effects of glacial load variability at up to daily temporal resolution and without seasonal gaps. Furthermore, the existing cGPS infrastructure provides us with a low-cost compliment to field-based measurements.

The utility of inverting GPS displacement measurements for changes in environmental loading has been well documented over the last several years. GPS-measured vertical displacements have been used to estimate terrestrial water storage [*Argus et al.*, 2014; *Borsa et al.*, 2014; *Fu et al.*, 2015] and winter snowpack [*Ouellette et al.*, 2013]. *Drouin et al.* [2016] computed average seasonal contributions by atmospheric, oceanic, and hydrologic (lake reservoir, snow-water equivalent, and glacial mass) loads to the vertical motion recorded by cGPS in Iceland. Here we investigate the utility of cGPS-measured displacements for estimating seasonally variable ice cap mass changes in Iceland using a simple least squares inversion. Throughout this work, we use ice cap mass to mean the total mass of the ice cap, including the mass of the snow that lies on top of the ice cap and any subglacial water bodies. We focus on analysis of motions on annual and shorter times scales, from 60 to 360 days, which record the Earth's elastic response to annual winter accumulation and spring melt seasons, and we perform additional analysis of year-to-year variability. We take advantage of all three components of cGPS-recorded motion, noting that the annual periodic motion in the horizontal is a direct result of environmental loading and free of tectonic signals. We discuss the impacts of atmospheric, hydrologic, and nontidal ocean loading on the GPS displacement time series. Our goal is to provide a mass variation time series to compliment other methods and to take advantage of the substantial increase in temporal resolution that cGPS allows.

2. cGPS Data

We analyzed all available data from 62 cGPS stations in Iceland (Figure 1 and Table 1) for the 10 year period 2004–2014 together with >100 globally distributed reference stations using the GAMIT/GLOBK GPS processing software version 10.4 [*Herring et al.*, 2010a,b]. We used International GNSS Service (IGS) IGS05 absolute phase center and FES2004 ocean loading models [*Lyard et al.*, 2006] and estimated corrections to a priori estimates of orbital parameters and Earth orientation. All time series presented here are relative to the ITRF2008 reference frame [*Altamimi et al.*, 2011]. Prior to correcting the time series for the effects of non-ice cap environmental loading (described below), we visually inspected each time series to identify breaks and to remove data from time periods overly contaminated by tectonic or volcanic signals such as the 2008 South Iceland Seismic Zone earthquake [*Hreinsdóttir et al.*, 2009] and the 2010 eruption of Eyjafjallajökull [*Sigmundsson et al.*, 2010]. We have excluded data after 2014 to avoid contaminating signals from
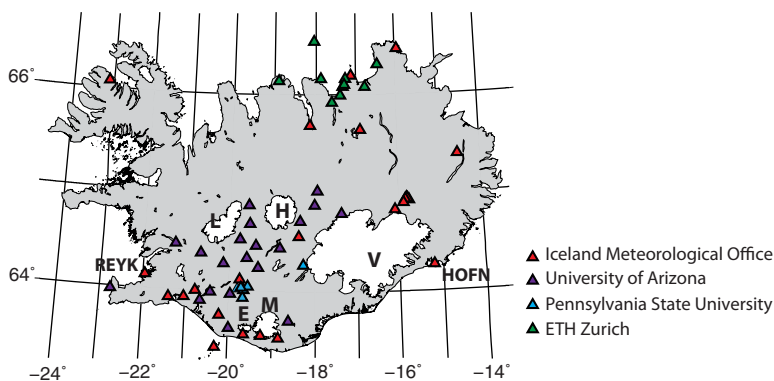
Figure 1. Locations of GPS stations used in this study. Parties supplying the GPS hardware are indicated by the symbol colors. Installation and operation of the sites used in this study were led by the Icelandic Meteorological Office (IMO), University of Iceland, University of Arizona, Penn State, ETH, Landmælingar Íslands, Landsvirkjun, Université de Savoie, Bayerische Akademie der Wissenschaften and KAUST. REYK and HOFN are International GNSS Service (IGS) stations. V = Vatnajökull, H = Hofsjökull, L = Langjökull, M = Mýrdalsjökull, E = Eyjafjallajökull. Station information is listed by site in Table 1.

the Holuhraun rifting event [*Sigmundsson et al.*, 2014], which was recorded by a large majority of cGPS stations in Iceland.

2.1. Time Series Corrections

For this investigation, we are only interested in the short-term periodic crustal motions related to snow accumulation and melting on the ice caps. *Compton et al.* [2015] showed that cGPS stations in Iceland experience measurable uplift accelerations in the vertical coordinate component. Rather than simultaneously incorporating parameters for initial offsets, velocities, and accelerations in our ice mass inversion scheme, we instead estimated these parameters and used these estimates to reduce the time series such that the residuals exhibit zero mean quasiperiodic motions without secular trends. This simplifies the inversion, as we can assume that the Earth behaves elastically on this time scale.

Additionally, while it has been shown that the majority of annual motion in Iceland is likely due to loading of the major ice caps [e.g., *Grapenthin et al.*, 2006; *Pinel et al.*, 2007], recent work demonstrates that displacements associated with atmospheric pressure, continental water storage, and nontidal ocean loading are nonnegligible and recorded by cGPS [*Drouin et al.*, 2016]. We computed surface displacements due to these environmental loads, removed them from our cGPS time series (Figure 2), and explored the impact of such a reduction on our inversion results. Hereafter, we refer to those time series from which non-ice environmental loading effects have been removed as the reduced time series.

We computed the surface displacements due to atmospheric pressure (ATML), continental water storage (CWS), and nontidal ocean loading (OBP) using the methods outlined in *van Dam and Wahr* [1987] for atmospheric pressure loading. We convolved global grids of the surface masses described below with Farrell's Green's functions for mass loading [*Farrell*, 1972] over a Gutenberg-Bullen Earth model.

Changes in atmospheric pressure were derived from the National Center for Environmental Prediction's (NCEP) 6 hourly reanalysis surface pressure. The data are provided every 2.5° in latitude and longitude [*Kalnay et al.*, 1996]. When modeling ATML, we must consider the response of the ocean to atmospheric pressure, and in this case we use a modified inverted barometer, wherein we take the net mass change over the oceans and divide by the area of the ocean basin [*van Dam and Wahr*, 1987].

Surface mass changes associated with continental water storage were generated using the Noah-version 1 GLDAS model [*Rodell et al.*, 2004; *Rui*, 2011]. These monthly grids (1.0° in longitude and latitude) provide estimates of snow water equivalent and soil moisture for those pixels not classified as permanent ice in the NOAHv3.3 vegetation data set, thus excluding load changes due to snow accumulation and melting on the ice caps.

The nontidal ocean loading effects are derived using data from the ECCO Consortium (Estimating the Circulation and Climate of the Ocean: http://www.ecco-group.org/). We used the Jet Propulsion Laboratory's Kalman Filter (kf080) ocean bottom pressure products from the ECCO Kalman Filter series [*Fukumori*, 2002].

Table 1. cGPS Station Information

Site ID	Longitude (°)	Latitude (°)	Start Date	N[a]	Data Density (%)
AKUR	341.878	65.685	2001.6	3194	70.4
ARHO	342.891	66.193	2002.6	3495	84.1
BALD	344.251	64.924	2008	1598	73.5
BRUJ	343.912	64.829	2005.7	1139	37.6
BUDH	340.675	64.240	2006.6	2577	95.8
DYNC	342.634	64.791	2008.7	1804	92.4
FITC	340.408	64.337	2007.6	1178	50.6
FJOC	341.994	64.875	2007.7	2156	93.3
FTEY	342.152	66.160	2007.8	1911	84.4
GAKE	343.235	66.078	2006.9	2198	84.2
GLER	340.198	64.023	2006.9	1806	65.0
GMEY	341.981	66.539	2007.5	1476	62.4
GOLA	340.678	63.660	2006.2	2088	73.3
GRAN	342.421	65.919	2006.7	2204	82.9
GRVA	340.616	64.464	2011.4	644	69.1
HAHV	344.191	64.949	2008.5	1589	78.4
HAMR	340.014	63.622	2000.5	1170	23.7
HAUC	341.655	64.711	2007.7	2002	86.6
HAUD	340.036	63.969	2006.9	1965	75.7
HEDI	342.691	66.081	2007.2	2214	88.8
HEID	345.459	65.381	2006.6	966	35.8
HEKR	340.342	64.012	2007.8	1640	72.9
HESA	340.439	64.047	2006.9	1340	51.7
HLFJ	339.864	64.277	2006.6	1951	72.6
HLID	338.610	63.921	2000.5	4221	85.4
HOFN	344.802	64.267	1997.5	5833	96.8
HOTJ	342.756	66.162	2007.2	1925	77.2
HVEL	340.439	64.873	2006.6	1442	53.4
HVOL	341.152	63.526	2000.5	4038	81.6
INSK	340.466	64.683	2008.6	806	41.0
INTA	344.217	64.940	2008.3	2010	97.0
ISAF	336.881	66.074	2009.6	791	49.3
ISAK	340.253	64.119	2002	3915	89.5
JOKU	341.760	64.310	2001.4	557	11.3
KALT	339.344	63.897	2007.1	2007	79.0
KARV	344.160	64.933	2005.7	1469	48.5
KIDC	342.058	65.019	2007.7	2015	87.1
KIDJ	339.225	63.997	2001.1	4061	86.0
KOSK	343.557	66.303	2006.9	1671	64.0
KVIS	342.728	66.101	2007.2	1519	60.9
LFEL	340.241	64.526	2006.6	1845	68.5
MJSK	340.328	63.933	2006.9	1457	55.8
MYVA	343.109	65.642	2006.7	1025	38.3
NORS	340.283	64.035	2006.8	1631	61.5
NYLA	337.262	63.974	2006.6	2478	91.3
REYK	338.045	64.139	1996.1	6109	93.2
REYZ	338.045	64.139	2001	2430	51.2
RHOF	344.053	66.461	2001.6	3126	68.7
SARP	338.734	64.467	2008.7	1224	62.9
SAUD	344.116	64.898	2004.8	2205	65.8
SAUR	339.575	63.984	2007.1	2177	85.9
SAVI	342.624	65.993	2007.7	1682	72.7
SELF	338.968	63.929	2002.1	3511	80.8
SIFJ	341.101	66.138	2007.5	2047	86.3
SKDA	339.334	64.377	2008.7	1354	69.3
SKRO	341.622	64.557	2000.7	4003	82.6
SNAE	341.368	63.736	2007.2	1029	41.3
SOHO	340.753	63.552	2000.5	3611	73.1
STKA	341.178	64.439	2006.6	2451	91.1
STOR	339.788	63.753	2005.1	2621	80.3
THEY	340.357	63.561	2000.5	3792	76.8
VMEY	339.706	63.427	2000.6	4122	84.0

[a]Because we allow gaps to remain in the data, N, the number of daily position estimates, provides a measure of data density for each cGPS site when considered in combination with the site start date. Data density is calculated as the number of daily position estimates relative to the total number of days from the site start date through 31 December 2013.
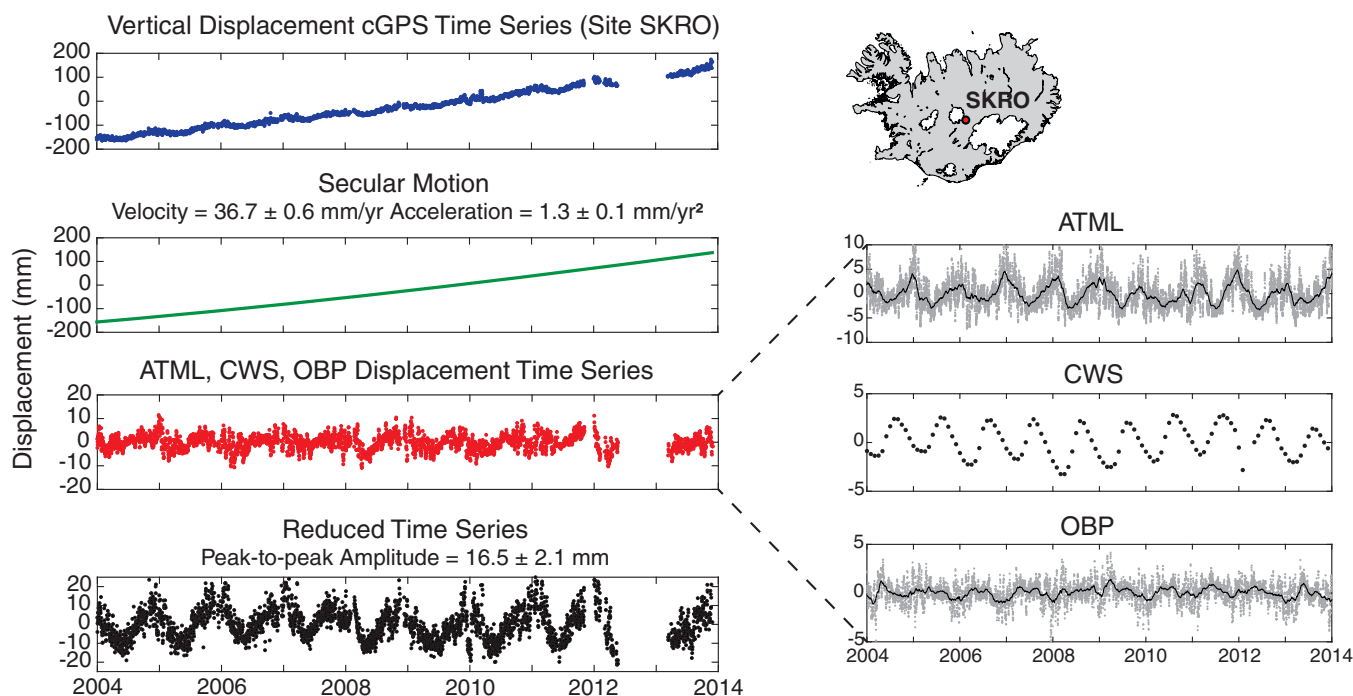
Figure 2. Time series filtering. Before inversion, we remove the secular velocity and acceleration as well as computed displacements due to atmospheric pressure (ATML), continental water storage (CWS), and nontidal ocean loading (OBP) from the cGPS displacement time series. Here we show the effects of these corrections on the vertical component of motion for site SKRO located in central Iceland between the Vatnajökull and Hofsjökull ice caps. Sixty day running means are plotted on top of the raw ATML and OBP time series to highlight the displacement amplitudes and periodicity. Prior to correction the vertical seasonal amplitude for site SKRO is 19.4 ± 2.4 mm.

The OBP is produced twice daily at 0600 and 1800 h between 78.5°N latitude to 79.5°S latitude over the global oceans. Longitudinal spacing is 1° globally. In latitude, the spacing between the product's northern limit and 20° of the equator is 1° and is gradually reduced to 0.3° within 10° of the equator. As part of the preprocessing, we interpolated the ECCO data to 1° spacing in latitude and longitude. Long-term trends exist in the ECCO OBP data because oceanic volume, rather than mass, is held constant in the ocean general circulation model. Therefore, we removed a mean and a long-term trend from the ECCO data.

To ensure that the surface displacements predicted from the mass loading are consistent with the reference frame in which the GPS time series are realized, we computed the Green's functions with respect to a center of figure frame (CF). *Dong et al.* [2003] found that GPS network solutions that have been transformed into the ITRF are in a frame that approximates the center of figure (CF) of the Earth on seasonal time scales (see *Blewitt* [2003] and *Dong et al.* [2003] for a thorough discussion of the GPS reference frame).

We find that the sum of the predicted annual displacements due to ATML, CWS, and OBP loading are largely in phase with the GPS-observed motions (for a more in depth examination of the regional patterns of the amplitude and phase of these loads see *Drouin et al.* [2016]). Although in some years, there is a slight phase offset in peak displacement between the raw cGPS time series and the displacement due to ATML, CWS, and OBP loading, the reduced cGPS time series show no phase shift relative to the original time series (Figure 2). To examine the impact that ATML, CWS, and OBP reduction has on the cGPS annual amplitudes, we solved for the amplitude of an annual sinusoidal fit for each component of cGPS motion for both the reduced and original data sets. We find that non-ice cap environmental load reduction results in smaller magnitude peak-to-peak vertical amplitudes by an average of 2.7 mm and a reduction in amplitude uncertainty estimates by an average of 0.2 mm across the network. Horizontal amplitudes appear relatively unaffected with an average increase of only 0.1 mm (with an 0.06 mm increase and 0.02 mm decrease in amplitude uncertainty estimates for north and east, respectively), but we do note the subtle rotation of peak-to-peak horizontal motion, especially for sites on the south coast (Figure 3).
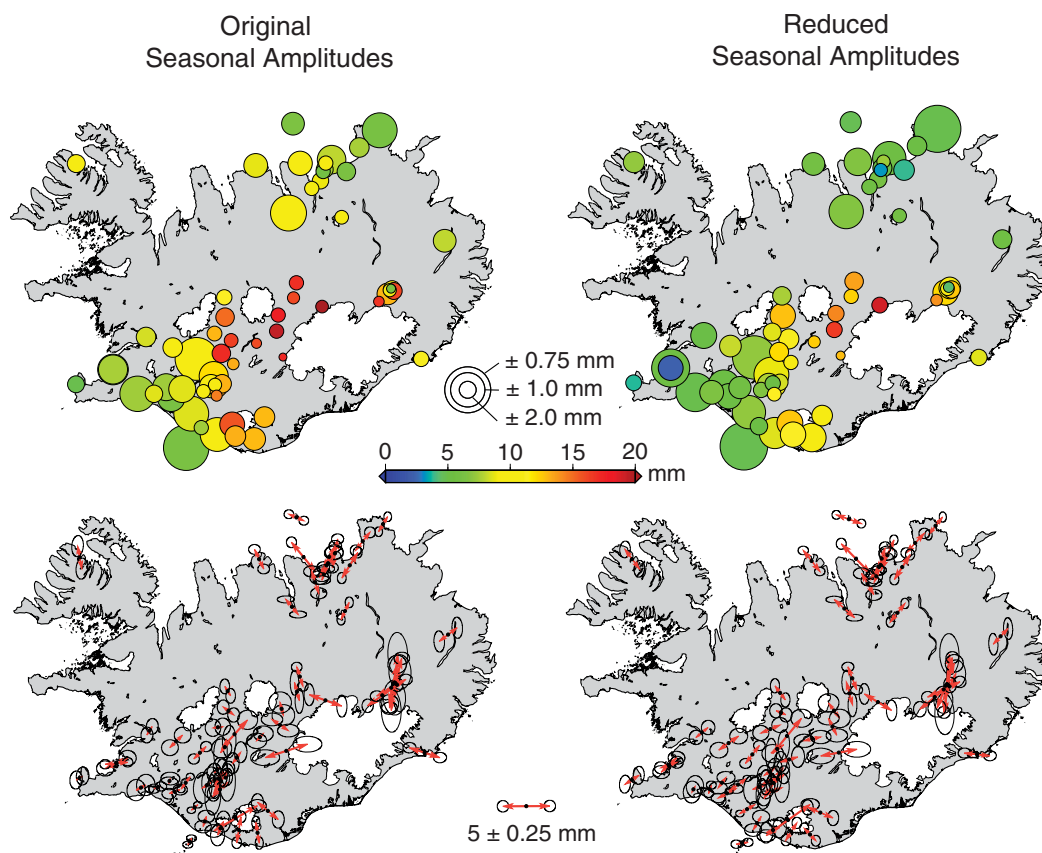
Figure 3. Seasonal amplitudes. Amplitudes of cGPS-measured seasonal peak-to-peak ground motion in the vertical (top) and horizontal (bottom) components before (left-hand side) and after (right-hand side) removing seasonal displacements due to loading by ocean bottom pressure, atmospheric pressure, and continental water storage (values reported in Table 2). In the vertical, the color bar indicates magnitude, while the size of the symbol is inversely proportional to the uncertainty of the amplitude estimate.

2.2. Regional Patterns of Seasonal Motion

Our estimates of vertical annual motion from the raw cGPS time series generally agree with previous studies [*Grapenthin et al.*, 2006]. Spatial variation in the amplitudes is similar to the patterns of secular vertical velocities [*Árnadóttir et al.*, 2009; *Geirsson et al.*, 2010] and accelerations [*Compton et al.*, 2015] with larger amplitudes in the center of Iceland that decrease toward the coasts. Assuming that seasonal motions are sinusoidal, we estimate amplitudes of vertical peak-to-peak periodic displacements as high as 22 mm (18 mm for the reduced data set) in the Central Highlands region of the island between the Vatnajökull and Hofsjökull ice caps (Figure 3 and Table 2). Amplitudes decrease with distance from the ice caps to <5 mm on the north and southwest coasts.

Horizontal motions show peak-to-peak amplitudes of over 5 mm at some sites. Sites in southern Iceland show the expected pattern of horizontal motion oriented perpendicular to the nearest ice cap edge. However, in central Iceland, superposition of the responses to loading on each ice cap result in seasonal motion orientations rotated relative to the expected direction from either ice cap. This phenomenon is especially apparent between the Vatnajökull and Hofsjökull ice cap where it is clear that the response to loading on Vatnajökull dominates the signal. The orientations of seasonal motion for sites to the northeast and due south of Hofsjökull are nearly parallel to the edge of that ice cap, largely aligned instead with the expected motions from Vatnajökull (Figure 3).

3. Inversion Method

We perform a simple weighted least squares inversion independently for each epoch for which there are position estimates from at least 15 GPS sites such that

Table 2. Time-Averaged cGPS-Observed Seasonal Amplitudes

	Original cGPS Seasonal Amplitudes (mm)[a]			Reduced cGPS Seasonal Amplitudes (mm)		
Site ID	Vertical	North	East	Vertical	North	East
AKUR	9.8 ± 1.0	1.6 ± 0.3	1.3 ± 0.7	6.7 ± 1.0	2.0 ± 0.3	2.2 ± 0.7
ARHO	8.0 ± 1.2	3.1 ± 0.4	0.6 ± 0.5	5.5 ± 1.0	3.2 ± 0.4	1.4 ± 0.4
BALD	16.1 ± 2.0	2.7 ± 1.5	0.7 ± 1.0	12.6 ± 2.0	2.7 ± 1.2	1.5 ± 0.8
BRUJ	16.7 ± 3.2	2.1 ± 0.6	3.2 ± 0.5	13.9 ± 2.9	4.2 ± 4.2	0.3 ± 0.6
BUDH	13.3 ± 2.9	1.2 ± 0.9	0.8 ± 0.5	9.8 ± 2.4	9.1 ± 3.1	1.9 ± 0.6
DYNC	22.8 ± 2.7	1.3 ± 1.0	3.5 ± 0.4	18.9 ± 2.2	1.8 ± 0.9	2.9 ± 0.5
FITC	17.1 ± 1.9	1.2 ± 1.4	0.9 ± 0.6	12.0 ± 1.8	0.9 ± 1.3	1.3 ± 0.5
FJOC	16.0 ± 2.8	1.9 ± 1.1	0.5 ± 0.4	12.3 ± 2.4	2.4 ± 1.0	0.7 ± 0.4
FTEY	9.2 ± 1.4	3.2 ± 0.5	2.6 ± 0.4	6.7 ± 1.3	3.3 ± 0.5	3.2 ± 0.4
GAKE	6.4 ± 1.9	2.7 ± 0.5	1.8 ± 0.4	3.8 ± 1.7	2.6 ± 0.5	1.7 ± 0.4
GLER	10.4 ± 1.5	0.2 ± 0.5	0.5 ± 0.3	7.8 ± 1.5	0.6 ± 0.5	1.0 ± 0.3
GMEY	6.5 ± 1.5	0.7 ± 0.4	1.6 ± 0.4	4.8 ± 1.6	1.0 ± 0.4	2.7 ± 0.4
GOLA	15.7 ± 1.4	2.7 ± 0.6	4.6 ± 0.8	12.6 ± 1.3	3.4 ± 0.5	4.6 ± 0.8
GRAN	8.9 ± 2.4	2.4 ± 0.5	0.7 ± 0.7	5.6 ± 2.2	2.3 ± 0.5	1.3 ± 0.7
GRVA	16.3 ± 2.5	3.1 ± 0.8	2.7 ± 0.9	11.1 ± 1.7	3.8 ± 0.8	3.0 ± 0.9
HAHV	6.3 ± 3.8	5.9 ± 1.9	0.9 ± 0.9	4.3 ± 3.2	6.4 ± 1.8	0.7 ± 0.8
HAMR	7.4 ± 2.4	1.1 ± 0.5	0.3 ± 0.7	5.1 ± 2.0	1.5 ± 0.6	0.8 ± 0.7
HAUC	17.7 ± 2.4	1.4 ± 0.9	0.4 ± 1.0	14.2 ± 2.1	1.7 ± 0.8	1.2 ± 0.9
HAUD	10.3 ± 2.5	0.6 ± 1.4	0.9 ± 0.8	6.6 ± 2.2	0.6 ± 1.2	1.4 ± 0.8
HEDI	5.9 ± 2.4	2.6 ± 0.6	1.6 ± 0.8	3.2 ± 2.6	2.8 ± 0.5	2.0 ± 0.8
HEID	8.0 ± 1.5	1.3 ± 0.9	2.0 ± 0.5	5.6 ± 1.8	1.6 ± 1.0	1.7 ± 0.4
HEKR	13.5 ± 1.8	2.7 ± 0.6	1.6 ± 0.5	10.0 ± 1.7	3.3 ± 0.6	1.9 ± 0.5
HESA	13.1 ± 1.9	0.2 ± 0.8	0.3 ± 0.5	8.3 ± 2.1	1.0 ± 0.8	1.3 ± 0.5
HLFJ	9.5 ± 0.8	1.4 ± 0.4	1.3 ± 0.5	7.1 ± 0.8	1.9 ± 0.4	1.4 ± 0.5
HLID	7.4 ± 1.0	0.6 ± 0.9	1.0 ± 0.8	4.9 ± 0.9	0.6 ± 1.0	0.3 ± 0.7
HOFN	11.1 ± 2.2	1.2 ± 0.5	3.2 ± 0.6	8.6 ± 2.1	0.4 ± 0.4	2.7 ± 0.6
HOTJ	10.0 ± 2.4	2.3 ± 0.5	1.3 ± 0.5	7.3 ± 2.6	2.3 ± 0.5	0.8 ± 0.5
HVEL	11.4 ± 2.3	1.0 ± 0.6	0.7 ± 0.4	7.6 ± 1.8	1.5 ± 0.6	1.2 ± 0.4
HVOL	12.9 ± 1.5	2.2 ± 0.5	0.4 ± 0.3	10.7 ± 1.2	1.3 ± 0.5	1.3 ± 0.4
INSK	15.0 ± 1.8	0.8 ± 0.6	1.1 ± 0.5	12.7 ± 1.3	0.4 ± 0.6	1.1 ± 0.5
INTA	11.1 ± 2.0	5.3 ± 0.5	1.5 ± 0.7	9.7 ± 1.6	5.8 ± 0.5	1.1 ± 0.5
ISAF	9.2 ± 2.0	2.4 ± 0.9	0.7 ± 0.5	7.1 ± 1.6	1.9 ± 0.7	1.7 ± 0.5
ISAK	12.0 ± 1.2	0.7 ± 0.8	0.6 ± 0.6	8.8 ± 1.0	0.8 ± 0.9	1.1 ± 0.6
JOKU	17.3 ± 4.2	1.4 ± 0.7	4.5 ± 1.3	12.8 ± 3.8	0.7 ± 0.7	3.9 ± 1.2
KALT	6.3 ± 1.2	0.5 ± 0.5	1.2 ± 0.6	5.3 ± 1.4	1.1 ± 0.4	1.9 ± 0.6
KARV	10.7 ± 2.5	4.2 ± 0.8	1.0 ± 0.8	9.6 ± 2.5	4.7 ± 0.8	2.0 ± 0.8
KIDC	16.9 ± 2.4	2.0 ± 0.4	0.6 ± 0.5	13.5 ± 1.8	2.5 ± 0.4	0.9 ± 0.5
KIDJ	7.4 ± 1.3	0.5 ± 0.6	0.1 ± 0.8	5.4 ± 1.1	1.1 ± 0.5	0.8 ± 0.8
KOSK	7.6 ± 1.7	1.8 ± 0.5	1.6 ± 0.5	5.3 ± 1.7	2.0 ± 0.4	2.0 ± 0.5
KVIS	7.6 ± 2.0	2.3 ± 0.6	1.3 ± 0.8	5.1 ± 1.8	2.5 ± 0.6	1.4 ± 0.7
LFEL	13.0 ± 2.3	0.1 ± 0.8	1.0 ± 0.7	8.6 ± 1.9	0.9 ± 0.7	2.0 ± 0.7
MJSK	14.4 ± 3.1	1.5 ± 1.6	1.5 ± 0.7	11.4 ± 2.5	0.8 ± 1.3	2.0 ± 0.6
MYVA	9.0 ± 2.5	1.8 ± 0.5	0.9 ± 0.4	6.0 ± 2.2	1.9 ± 0.5	1.6 ± 0.4
NORS	9.6 ± 2.6	1.3 ± 1.2	0.7 ± 0.5	5.3 ± 2.2	0.4 ± 1.1	1.1 ± 0.5
NYLA	4.9 ± 2.0	0.5 ± 0.8	0.7 ± 0.5	3.7 ± 2.2	1.0 ± 0.8	1.4. ± 0.5
REYK	7.6 ± 1.2	1.2 ± 0.7	2.3± 0.8	5.6 ± 0.9	1.6 ± 0.6	1.5 ± 0.7
REYZ	4.6 ± 1.1	0.3 ± 0.4	2.4 ± 0.5	2.3 ± 1.4	0.7 ± 0.5	1.7 ± 0.6
RHOF	6.2 ± 1.0	1.6 ± 0.4	1.0 ± 0.3	4.9 ± 0.7	1.8 ± 0.4	1.6 ± 0.3
SARP	8.3 ± 1.7	0.9 ± 0.7	0.5 ± 0.5	5.0 ± 1.3	1.1 ± 0.6	1.2 ± 0.6
SAUD	13.0 ± 1.6	1.6 ± 0.5	3.2 ± 0.6	12.1 ± 1.4	1.5 ± 0.5	3.5 ± 0.5
SAUR	8.6 ± 1.3	1.4 ± 0.3	0.9 ± 0.4	5.8 ± 1.5	1.4 ± 0.3	1.9 ± 0.4
SAVI	8.8 ± 2.1	1.2 ± 0.4	0.5 ± 0.8	6.2 ± 2.0	1.3 ± 0.4	0.5 ± 0.7
SELF	8.6 ± 2.0	0.3 ± 0.4	0.7 ± 0.5	6.5 ± 1.5	0.9 ± 0.4	0.2 ± 0.4
SIFJ	8.7 ± 1.4	2.1 ± 0.4	1.0 ± 0.5	5.9 ± 1.5	2.2 ± 0.4	1.8 ± 0.5
SKDA	10.9 ± 1.8	1.4 ± 0.7	1.3 ± 0.7	8.2 ± 1.6	1.6. ± 0.7	2.0 ± 0.8
SKRO	19.4 ± 2.4	1.2 ± 0.6	1.7 ± 0.9	16.5 ± 2.1	1.8 ± 0.6	0.9 ± 0.9
SNAE	12.9 ± 1.6	1.8 ± 0.8	2.2 ± 0.5	10.2 ± 1.7	1.1 ± 0.7	2.7 ± 0.5
SOHO	13.1 ± 1.6	2.8 ± 0.5	0.4 ± 0.4	11.3 ± 1.4	1.9 ± 0.5	1.1 ± 0.4
STKA	15.9 ± 3.4	0.8 ± 0.7	0.7 ± 0.9	12.5 ± 2.8	0.4 ± 0.6	1.8 ± 0.9
STOR	8.5 ± 1.0	0.6 ± 0.3	0.7 ± 0.4	7.1 ± 1.0	1.0 ± 0.3	1.5 ± 0.4
THEY	10.1 ± 1.0	1.5 ± 0.9	0.6 ± 0.6	8.5 ± 1.1	0.6 ± 0.9	1.4 ± 0.6
VMEY	6.3 ± 0.8	0.7 ± 0.3	0.4 ± 0.4	4.8 ± 0.7	0.2 ± 0.4	1.3 ± 0.4

[a]Seasonal amplitudes are reported as peak-to-peak (full amplitude) displacements.

$$I = \left(A^T W A\right)^{-1} A^T W d, \qquad (1)$$

where the vector I represents the load estimates for each ice cap. I is determined from the daily cGPS position estimates, d, the calculated greens functions, A (described below), and weighted by the inverse of the daily cGPS variance matrix, W. Daily cGPS position uncertainties are derived from an analysis of postfit phase residuals computed by GAMIT wherein phase uncertainties are weighted by elevation angle. We do not consider spatially or temporally correlated data uncertainties in performing this calculation. Like Árnadóttir et al. [2009] and Schmidt et al. [2013], we group the Eyjafjallajökull and Mýrdalsjökull ice caps and thus solve for only four loading values at any given epoch. We invert each epoch independently; inversion results are not constrained to be similar to those at the previous epoch or to follow any predetermined curve. We also allow there to be gaps in the GPS time series and skip those epochs that do not meet the 15 site criteria. We have chosen the time period 2004–2014 to allow ourselves a long enough time span to test our inversion methods and to identify patterns in our results. 2004 is the first year where there are consistently 15 cGPS sites with data available for inversion.

Each cGPS position time series has a zero mean and provides information about the daily variations from some average position. Consequently, the computed ice mass variation time series provide insight into variations from the average ice cap mass over the same time period. Thus, we do not solve for total ice cap mass.

3.1. Load Green's Functions

To compute the load Green's functions for the inversion, it is first necessary to define an Earth model that adequately reproduces the annual amplitudes observed with cGPS. To do this, we compare our estimates of the average annual peak-to-peak amplitude for each cGPS time series with the modeled response to loading by the multiyear averages of winter mass balance for each ice cap compiled by Grapenthin et al. [2006] (Figure 4 and Table 3), noting that this assumes the timing of maximum loading is everywhere the same.
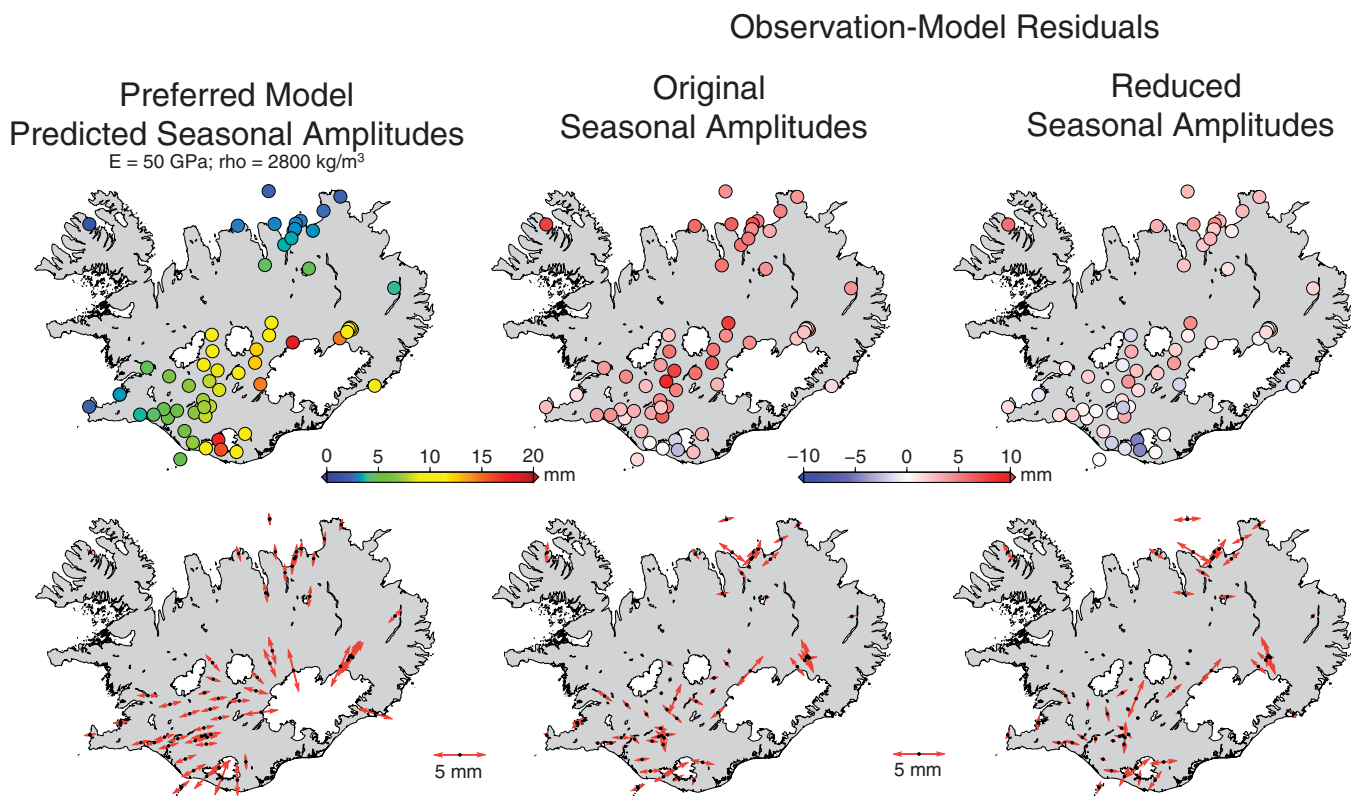
Figure 4. Preferred Earth model and GPS residuals. RELAX-computed responses to loading by the average winter mass balances (Table 3) and resulting misfit for the reduced and original cGPS-measured peak-to-peak amplitudes presented in Figure 3. Note that we have tuned our half-space model to fit the reduced cGPS amplitudes, so those residual values are much smaller, while the original cGPS amplitudes are almost all underestimated by the predicted displacements.

Table 3. Ice Cap Data

Glacier Group[a]	Area (km^2)	b_w (m$_{we}$)[b]
Vatnajökull, Tungnafellsjökull, Thrándarjökull, and Hofsjökull in Lón	8,520	1.5
Mýrdalsjökull, Eyjafjallajökull, Torfajökull, and Tindfjallajökull	836	2.5
Hofsjökull	976	1.25
Langjökull, Eiríksjökull, Thórisjökull, and Hrútfell	1,100	1.65
Total ice cap area	11,432	
Weighed average winter mass accumulation		1.57

[a]Glacier groupings and ice cap area used throughout this work follow that of *Schmidt et al.* [2013] and include the five largest ice caps in central Iceland and associated nearby glaciers. Throughout this work, these groups are referred to by their dominant ice cap name.
[b]Average winter mass accumulation in meters water equivalent compiled by *Grapenthin et al.* [2006]. These values are used as the maximum loads in modeling peak-to-peak ground displacement and computing the best fit elastic half-space model.

We apply these loads to the 2 × 2 km grid described in *Schmidt et al.* [2013], which includes smaller glaciers that we group with the nearest large ice cap (Table 3). We compute the displacement response to loading by approximating a homogeneous elastic half-space using the RELAX code [*Barbot and Fialko*, 2010; *Barbot*, 2011] with a model domain that extends 2560 km in both north and east directions and 1280 km in depth, large enough that we are confident that model boundary effects do not contaminate our results. Informed by previous work [*Grapenthin et al.*, 2006], we tested Young's moduli (E) from 30 to 55 GPa (in steps of 5 GPa, keeping Poisson's ratio constant at 0.25 throughout) and densities (ρ) of 2800, 2900, and 3000 kg/m^3 and compared the results to the time-averaged amplitudes for both our reduced and original data sets. We find that a Young's modulus of 50 GPa and density of 2800 kg/m^3 fit the amplitudes of our reduced data set best using a weighted sum-square misfit scheme to assess goodness of fit for all three components of motion, and this is the Earth model we use throughout our analysis (Figure 4 and Table 4). The slightly larger seasonal amplitudes of the original data set are better fit by an Earth model with Young's modulus of 45 GPa and density of 2800 kg/m^3. We elaborate on these findings in our discussion of Earth models below.

We chose to use one Earth model (E = 50 GPa; ρ = 2800 kg/m^3) for the inversion of both the reduced and original time series data sets so as to maintain consistency and explore the impact of the corrections on our inversion results. To create the Green's functions for our inversion, we computed the elastic responses to a 1 m water equivalent load for each of the four ice cap groups by prescribing a uniform load across the entire ice cap area (Table 3). We define the coordinate system such that a positive load value results in negative (downward) ground motion.

4. Results

Load variation time series are shown in units of water equivalent meters and smoothed by a 60 day running mean to damp high-frequency variation and highlight larger-scale features (Figure 6). We report uncertainties derived for each epoch from the diagonal elements of the computed variance-covariance matrix, $C = (A^T W A)^{-1}$, obtained from the inversion, which accounts for the varying number of sites available at each epoch, such that epochs with fewer data inputs have larger uncertainties. Three-hundred and three days in 2004 meet the 15-site criterion set in the inversion, and only 57 days from the 9 year period 2005–2014 are omitted due to a lack of data (Figure 5). We do not present uncertainties associated with the 60 day running mean loading histories nor do we employ a time-correlated error model to estimate uncertainties. Rather, we acknowledge that the uncertainties presented here and shown in Figure 6 may represent conservative error estimates.

4.1. Load Variation Time Series

We find that the Vatnajökull and Mýrdalsjökull/Eyjafjallajökull loading histories derived from the reduced time series roughly match a periodic signal with an amplitude representative of an average winter mass balance for each ice cap [*Grapenthin et al.*, 2006] and that the difference between the inversion results from the reduced and original data sets is not statistically significant (Figure 6).

The timing and magnitude of winter accumulation and spring melting is not expected to be identical from year to year and we find that our load-variation time series may capture such annual variability. For example, the *Iceland Meteorological Office* [2010] reported higher than average rates of precipitation in parts of the country for 2009, which may have led to increased accumulation on the ice caps [*Drouin et al.*, 2016] and the less than average mass loss in late-2009 observed for Vatnajökull (Figure 6). To evaluate the

Table 4. Model-Computed Seasonal Amplitudes[a]

Site ID[b]	Longitude (°)	Latitude (°)	Vertical (mm)	North (mm)	East (mm)
AKUR	**341.878**	**65.685**	**4.43**	**1.79**	**0.34**
ALFD	343.966	64.984	9.59	2.99	1.49
ARHO	**342.891**	**66.193**	**2.87**	**1.34**	**0.09**
AUST	340.919	63.674	18.87	0.95	0.99
BALD	**344.251**	**64.924**	**10.18**	**2.84**	**2.14**
BAS2	340.524	63.676	11.70	0.39	2.46
BASA	340.528	63.679	11.70	0.39	2.46
BAUG	342.665	66.038	3.31	1.49	0.03
BJAC	343.175	65.605	4.71	1.92	0.29
BLAC	338.347	63.962	3.47	0.41	1.47
BREC	338.236	63.974	3.34	0.39	1.43
BRUJ	**343.912**	**64.829**	**14.49**	**3.89**	**1.95**
BUDH	**340.675**	**64.240**	**8.40**	**0.37**	**1.76**
DAGF	340.200	63.628	8.53	1.13	2.78
DAGM	340.165	63.628	8.53	1.13	2.78
DRA2	338.586	64.049	3.86	0.40	1.58
DRAU	338.588	64.050	3.86	0.40	1.58
DYN2	342.634	64.791	18.47	4.06	0.98
DYNC	**342.634**	**64.791**	**18.49**	**4.06**	**0.98**
DYNG	343.348	65.056	9.83	3.25	0.60
DYNH	342.634	64.792	15.38	4.02	0.89
DYNY	342.884	65.016	10.71	3.41	0.07
ENTA	340.818	63.701	18.31	0.74	1.78
ENTC	340.818	63.701	18.31	0.74	1.78
EYVI	344.196	64.235	13.83	2.25	3.58
FEDG	340.311	64.025	7.45	0.38	1.92
FIM2	340.566	63.610	13.50	2.40	2.34
FIMM	340.562	63.607	13.50	2.40	2.34
FITC	**340.408**	**64.337**	**7.97**	**0.45**	**1.64**
FJOC	**341.994**	**64.875**	**11.57**	**2.69**	**1.15**
FTEY	**342.152**	**66.160**	**2.96**	**1.37**	**0.11**
GAKE	**343.235**	**66.078**	**3.16**	**1.43**	**0.19**
GEIC	338.469	63.948	3.61	0.43	1.50
GFEL	338.469	63.948	3.61	0.43	1.50
GFUM	342.733	64.407	26.41	0.11	0.67
GIGO	342.981	64.840	14.90	4.28	0.11
GJAC	342.386	64.829	13.58	3.25	1.29
GJAL	342.386	64.829	13.58	3.25	1.29
GLER	**340.198**	**64.023**	**7.14**	**0.43**	**1.92**
GMEY	**341.981**	**66.539**	**2.27**	**1.12**	**0.12**
GOLA	**340.678**	**63.660**	**17.41**	**1.49**	**2.19**
GRAN	**342.421**	**65.919**	**3.57**	**1.57**	**0.04**
GRFS	340.890	63.526	11.51	3.58	0.73
GRIM	342.729	64.407	26.41	0.11	0.67
GRVA	**340.616**	**64.464**	**8.75**	**0.25**	**1.59**
GSIG	343.322	64.678	21.09	3.29	1.07
GUSK	336.077	64.891	1.67	0.18	0.89
HAFS	342.178	64.480	21.37	1.12	2.82
HAHV	**344.191**	**64.949**	**9.40**	**2.72**	**1.97**
HAMR	**340.014**	**63.622**	**7.09**	**1.32**	**2.29**
HAUC	**341.655**	**64.711**	**12.47**	**1.20**	**1.20**
HAUD	**340.036**	**63.969**	**6.87**	**0.46**	**1.97**
HEDI	**342.691**	**66.081**	**3.20**	**1.45**	**0.03**
HEID	**345.459**	**65.381**	**3.82**	**1.18**	**1.25**
HEKR	**340.342**	**64.012**	**7.79**	**0.30**	**1.91**
HESA	**340.439**	**64.047**	**7.98**	**0.32**	**1.84**
HH25	338.583	64.067	3.86	0.40	1.58
HH25_G15	338.583	64.067	3.86	0.40	1.58
HLFJ	**339.864**	**64.277**	**6.99**	**0.66**	**1.76**
HLID	**338.610**	**63.921**	**3.71**	**0.48**	**1.52**
HOFN	**344.802**	**64.267**	**9.57**	**1.18**	**3.23**
HOTJ	**342.756**	**66.162**	**2.98**	**1.38**	**0.06**
HRIC	343.076	64.950	11.83	3.70	0.27
HRIM	343.076	64.950	11.83	3.70	0.27
HUSM	338.583	64.067	3.86	0.40	1.58
HVEL	**340.439**	**64.873**	**9.07**	**1.45**	**1.29**
HVER	338.815	64.017	4.13	0.47	1.62
HVHL	338.002	63.906	2.96	0.36	1.32

Table 4. (continued)

Site ID[b]	Longitude (°)	Latitude (°)	Vertical (mm)	North (mm)	East (mm)
HVOL	**341.152**	**63.526**	**10.31**	**3.07**	**0.08**
INSK	**340.466**	**64.683**	**9.61**	**0.39**	**1.28**
INTA	**344.217**	**64.940**	**9.40**	**2.72**	**1.97**
ISAF	**336.881**	**66.074**	**1.49**	**0.50**	**0.66**
ISAK	**340.253**	**64.119**	**7.40**	**0.43**	**1.80**
ISMA	338.999	63.938	4.35	0.57	1.65
JOKU	**341.760**	**64.310**	**14.47**	**0.42**	**3.27**
KAFC	338.516	64.061	3.70	0.38	1.55
KAFF	338.515	64.061	3.70	0.38	1.55
KALT	**339.344**	**63.897**	**4.94**	**0.61**	**1.75**
KALT	339.344	63.897	4.94	0.61	1.75
KARV	**344.160**	**64.933**	**9.76**	**2.89**	**1.86**
KIDC	**342.058**	**65.019**	**9.06**	**2.64**	**0.69**
KIDJ	**339.225**	**63.997**	**4.87**	**0.55**	**1.75**
KISA	342.438	64.674	20.65	3.09	1.98
KOSK	**343.557**	**66.303**	**2.62**	**1.24**	**0.23**
KRAC	343.225	65.694	4.32	1.80	0.27
KRBR	343.828	65.095	8.48	2.81	1.19
KRIV	337.923	63.878	2.93	0.38	1.30
KVEC	343.348	64.745	19.59	3.38	1.22
KVEF	343.311	64.674	21.09	3.29	1.07
KVIS	**342.728**	**66.101**	**3.08**	**1.41**	**0.06**
KVSK	343.567	63.982	13.13	3.66	1.92
LAMB	337.987	63.910	2.96	0.36	1.32
LANH	343.440	64.886	12.64	3.75	0.97
LFEL	**340.241**	**64.526**	**9.31**	**0.31**	**1.12**
MJSK	**340.328**	**63.933**	**8.17**	**0.22**	**2.02**
MOFC	343.333	64.984	10.66	3.42	0.64
MOFL	343.333	64.984	10.66	3.42	0.64
MOHA	337.940	63.920	2.96	0.36	1.32
MOHG	337.940	63.920	2.96	0.36	1.32
MORK	340.105	63.657	7.27	1.11	2.35
MYVA	**343.109**	**65.642**	**4.73**	**1.93**	**0.23**
NE63	338.657	64.040	4.02	0.42	1.62
NEFC	342.287	64.647	19.60	2.74	2.43
NORS	**340.283**	**64.035**	**7.40**	**0.39**	**1.87**
NYLA	**337.262**	**63.974**	**2.35**	**0.23**	**1.14**
OFE2	341.159	63.752	12.30	0.90	0.70
OFEL	341.159	63.752	12.30	0.90	0.70
OLKE	338.780	64.063	4.19	0.45	1.64
RENE	337.370	63.825	2.37	0.31	1.12
REYK	**338.045**	**64.139**	**3.23**	**0.24**	**1.43**
REYZ	**338.045**	**64.139**	**3.23**	**0.24**	**1.43**
RFEL	341.329	63.617	10.65	2.14	0.81
RHOF	**344.053**	**66.461**	**2.24**	**1.08**	**0.30**
RHOL	337.786	65.426	2.33	0.59	1.00
RIFC	343.612	64.925	12.13	3.54	1.24
RIFN	343.612	64.925	12.13	3.54	1.24
RJUC	342.473	64.743	18.81	3.56	1.86
RNES	337.347	63.825	2.37	0.31	1.12
RVIT	337.296	63.816	2.37	0.31	1.12
S001	337.294	63.829	2.37	0.31	1.12
SARP	**338.734**	**64.467**	**4.54**	**0.06**	**1.89**
SAUD	**344.116**	**64.898**	**10.62**	**3.01**	**2.02**
SAUR	**339.575**	**63.984**	**5.53**	**0.59**	**1.83**
SAVI	**342.624**	**65.993**	**3.44**	**1.54**	**0.03**
SELC	337.946	63.898	2.96	0.36	1.32
SELF	**338.968**	**63.929**	**4.35**	**0.56**	**1.66**
SENG	337.566	63.882	2.55	0.32	1.19
SIFJ	**341.101**	**66.138**	**2.89**	**1.28**	**0.38**
SJUK	342.660	66.049	3.31	1.49	0.03
SKDA	**339.334**	**64.377**	**6.32**	**0.58**	**2.09**
SKFC	343.011	64.026	15.30	3.81	0.00
SKOG	340.555	63.576	11.62	2.68	2.28
SKRO	**341.622**	**64.557**	**12.57**	**0.60**	**2.29**
SKSH	337.520	63.868	2.55	0.32	1.19
SMPI	338.647	64.016	3.96	0.45	1.59
SNAE	**341.368**	**63.736**	**10.00**	**1.43**	**0.13**

Table 4. (continued)

Site ID[b]	Longitude (°)	Latitude (°)	Vertical (mm)	North (mm)	East (mm)
SODU	340.414	63.963	7.93	0.31	1.96
SOHO	**340.753**	**63.552**	**15.83**	**3.35**	**1.28**
STE2	340.391	63.677	10.75	0.31	2.52
STEI	340.391	63.677	10.75	0.31	2.52
STKA	**341.178**	**64.439**	**10.41**	**0.11**	**2.02**
STOR	**339.788**	**63.753**	**5.80**	**0.82**	**1.96**
SVBH	340.381	63.580	13.00	2.13	2.71
SYRF	337.346	63.836	2.37	0.31	1.12
THEY	**340.357**	**63.561**	**9.73**	**2.47**	**2.35**
THOC	343.324	64.934	11.66	3.63	0.69
THOR	343.325	64.933	11.66	3.63	0.69
THRC	342.989	65.897	3.70	1.61	0.15
THRE	338.536	63.988	3.66	0.40	1.52
UPP2	343.694	65.029	9.29	3.02	1.15
URHA	342.853	64.820	16.56	4.26	0.61
URHC	342.853	64.820	16.56	4.26	0.61
VIKD	344.049	65.071	8.09	2.63	1.40
VMEY	**339.706**	**63.427**	**4.86**	**1.29**	**1.56**
VOGS	338.296	63.853	3.26	0.44	1.39
VONC	342.246	64.674	16.86	2.94	2.14

[a]Model-computed seasonal amplitudes are reported as peak-to-peak (full amplitude) displacement responses using the preferred Earth model described in the text and loading values reported in Table 3.
[b]cGPS sites used in this analysis are reported in bold and plotted in Figure 4. Model-computed seasonal amplitudes for additional sites, including continuous and semicontinuous GPS installations, are also reported for the readers' reference.

deviations we infer from perfectly periodic motion, we compare our Vatnajökull loading time series with seasonal stake measurements [*Björnsson et al.*, 2013]. To isolate the seasonal component of loading from the long-term mass loss observed for Vatnajökull, we have removed a secular trend from the summer mass balance observations. We find that the mass balance observations fall within the one-sigma uncertainty bounds of the load variation time series derived from both our reduced and original data sets (Figure 6). Thus, although we do not currently have the ability to independently model the amplitudes of deformation due to our limited understanding of the Icelandic elastic rheology (we use the amplitudes, rather, to tune our Earth model and thus recover those same amplitudes in our inversion), the interannual variability is nevertheless well captured. We computed the root mean square difference between the seasonal stake measurements for Vatnajökull and (1) the maximum/minimum values from the sinusoidal model based on average winter loading and (2) the load variation time series we have estimated from the cGPS. Since the inversion process does not require the results to be perfectly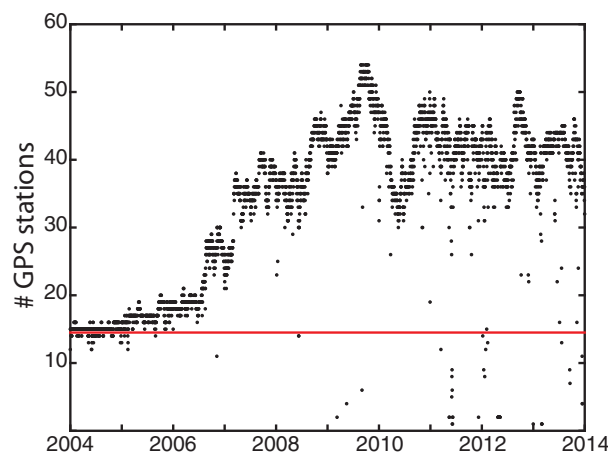 periodic, we do not compare values from a specific epoch but rather choose the maximum and minimum values for each season from our 60 day smoothed time series for the RMS comparison. Although there are few stake measurements with which to compare, we find that our cGPS-derived load variation time series represents a small reduction in RMS (RMS = 0.16 m_{we}) relative to the sinusoidal model (RMS = 0.21 m_{we}).

4.2. Load Variation Uncertainties

The uncertainties in our estimates primarily reflect the spatial configuration of the cGPS network. We find that the Vatnajökull and Mýrdalsjökull/Eyjafjallajökull have relatively well constrained ice load histories with average uncertainties of 0.3 and 1.1 m_{we}, respectively (Figure 6), whereas Hofsjökull and Langjökull ice histories are
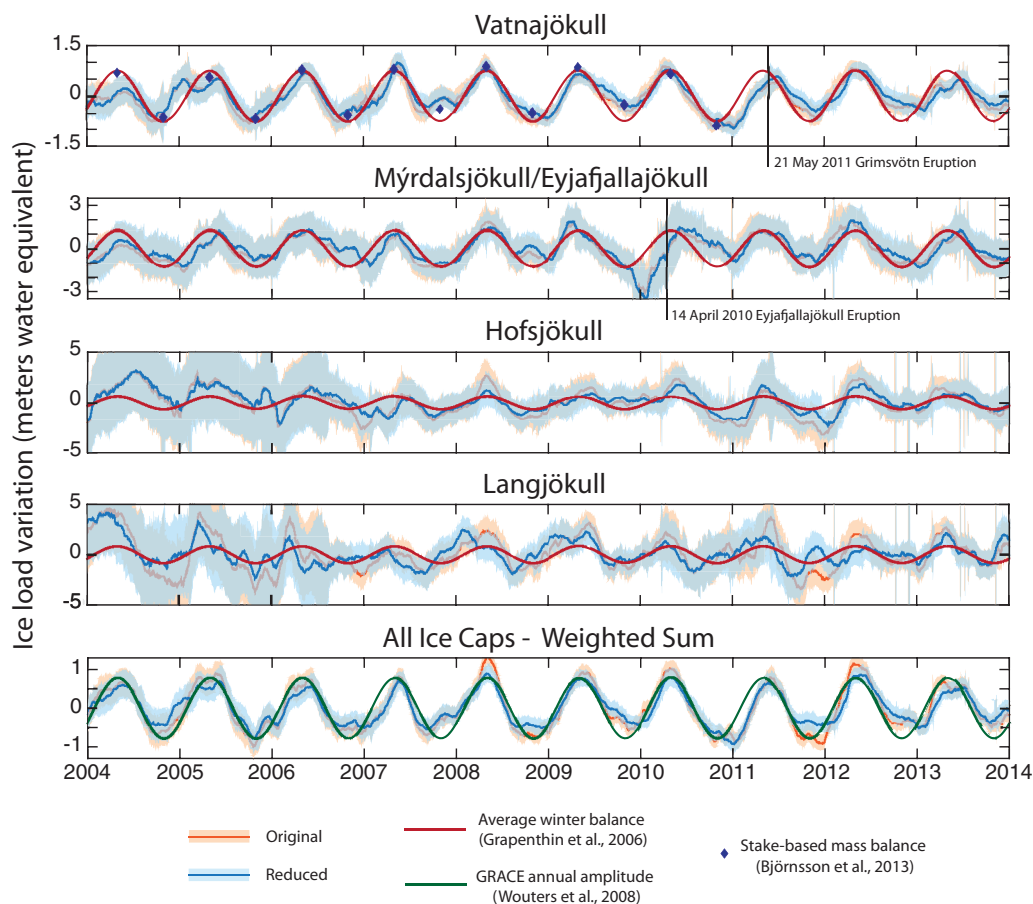

Figure 5. Number of GPS stations with data for each day between 2004 and 2014. Days for which there were fewer than 15 GPS stations online (below red line) were not included in the inversion. Note the dramatic uptick in available data starting in mid-2006 coincides with the reduction in uncertainties for the Hofsjökull and Langjökull ice histories (Figure 6).

Figure 6. Ice cap loading inversion results. 1σ uncertainties shaded for inversions using original and reduced cGPS data sets. Vatnajökull results match seasonal stake measurements (diamonds) [*Björnsson et al.*, 2013]. The weighed average annual winter balance from *Grapenthin et al.* [2006] is plotted for the sum load variation time series for all ice caps but is so similar to the amplitude derived from GRACE that it is hidden.

less well constrained, with average uncertainties of 2.1 and 2.0 m_{we}, respectively, due to the limited cGPS station distribution surrounding these ice caps. Station density in the Central Highlands region increased dramatically starting in mid-2006 [*Geirsson et al.*, 2010] (Figure 5), the result of which is a drop in the inversion uncertainty associated with the ice load estimates from this time forward (Figure 6). Uncertainties for Hofsjökull and Langjökull after 2006.5 are lower—1.6 and 1.5 m_{we}, respectively—but nevertheless remain high and are on the same order as the average annual winter balance for each ice cap (1.25 and 1.65 m_{we}, respectively; Table 3). Thus, the current distribution of stations in the existing cGPS network limits our ability to independently resolve ice-loading histories for these two ice caps.

A summary of the ice load variation time series weighted by the ice cap area is shown in Figure 6 and matches the annual amplitude for Iceland as a whole as observed by GRACE (half amplitude $= 8.9 \pm 3$ Gt/yr $= 0.7785$ m_{we}/yr [*Wouters et al.*, 2008]). The average uncertainty is 0.2 m_{we} for the time period 2006.5–2014 (Figure 6).

4.3. Impacts of Volcanic Activity

The 2010 Eyjafjallajökull and 2011 Grímsvötn eruptions present us with an opportunity to examine the impacts of volcanic events on both our inversion method as well as the seasonal ice cap load history estimates. In early 2010, seismicity and rapid uplift was detected near the Eyjafjallajökull volcano indicating magma inflation prior to an effusive flank eruption from 20 March to 12 April 2010, which was followed soon after by an explosive eruption beginning on 14 April 2010 [*Sigmundsson et al.*, 2010]. cGPS stations in southern Iceland recorded this unrest and we decided to filter out the position estimates for the inflation and eruption time period. We removed position estimates from the time series for sites falling within or

near the study area of *Sigmundsson et al.* [2010] for which these volcanic signals were readily apparent, including data from mid-2009 forward for station THEY [*Sigmundsson et al.*, 2010]. Despite removing the apparent volcanic signal from these time series, our loading time series inversion result for Mýrdalsjökull/ Eyjafjallajökull shows a dramatic drop of approximately 2 m_{we} between ~2009.9 and 2010.1 (Figure 6) with an average uncertainty from 2009.9 and 2010.5 of 1.5 m_{we}, 0.4 m_{we} higher than the average uncertainty for the whole time series. We are reluctant to interpret this large jump in the load variation time series as representing a meaningful change in mass. It is interesting to note, however, that the dramatic deviation in our load variation estimates, while out of phase and slightly preceding the main eruption in April, is coincident with the timing of magma intrusion and inflation starting in early 2010 [*Sigmundsson et al.*, 2010]. Thus, it is likely that this jump is the result of some combination of poor station coverage for the Mýrdalsjökull/Eyjafjallajökull ice caps resulting from our filtering of near-field data affected by volcanic signals and the impact of far-field motions [*Geirsson et. al*, 2015; S. Hjaltadóttir, personal communication, 2017].

Although the large negative jump in early-2010 is likely not a mass-change signal, we may resolve the effects of insulation and altered surface albedo due to tephra deposition on the Mýrdalsjökull/Eyjafjallajökull and Vatnajökull ice caps following the 2010 Eyjafjallajökull eruption [*Gudmundsson et al.*, 2012; *Björnsson et al.*, 2013]. Our Mýrdalsjökull/Eyjafjallajökull load variation time series shows mass loss in the second half of 2010 that lags an annual periodic sinusoid by ~2 months. We also note that the seasonal minimum in early 2011 is −0.89 m_{we}, 0.36 m_{we} greater than the average value of −1.25 m_{we}. Although we cannot rule out that precipitation or temperature variations contribute to the observations, we interpret these results to indicate that the Mýrdalsjökull/Eyjafjallajökull ice cap was delayed in melting and lost less mass than usual in the summer and fall following the Eyjafjallajökull eruption due to the insulating effects of the thick tephra deposits over all of Eyjafjallajökull and a large portion of the Mýrdalsjökull ice cap [*Gudmundsson et al.*, 2011, 2012; *Jóhannesson et al.*, 2013; *Dragosics et al.*, 2016]. Ablation rates of Icelandic ice are reduced due to the insulation effects of a layer of insulating ash greater than approximately 10 mm [*Nield et al.*, 2012; *Dragosics et al.*, 2016; *Möller et al.*, 2016]. Tephra fallout from the 2010 eruption resulted in a continuous tephra blanket up to 80 km distance from the eruptive center, and within 2 km of the source vents, tephra deposits measured between 1 and 30 m [*Gudmundsson et al.*, 2011, 2012].

Relatedly, the Vatnajökull load variation time series shows a larger than average summer mass drop and a longer than average melting season in 2010, and in early-2011, mass gain from winter snows lags the average timing by ~2 months. The large mass loss in 2010 recorded by stake mass balance field campaigns for the Vatnajökull, Hofsjökull, and Langjökull ice caps has been interpreted as a direct result of deposition of a thin layer of tephra and reduced surface albedo [*Björnsson et al.*, 2013]. Here with the increase in temporal resolution afforded by cGPS, we are able to recover the timing of that mass loss from the Vatnajökull ice cap, and the character and timing of the mass recovery the following winter.

The Hofsjökull and Langjökull ice histories both show negative deviations from the mean seasonal minima in 2011 but are not well enough resolved to be significant indicators of albedo-related melting due to the 2010 Eyjafjallajökull eruption. However, it is possible that if cGPS station density were higher in this region, we would have been able to resolve the effects of tephra deposition on the Hofsjökull and Langjökull ice caps [*Gudmundsson et al.*, 2012] and the well documented dramatic increase in melt rates for the Langjökull ice cap of nearly double [*Björnsson et al.*, 2013].

Our load time series for Vatnajökull may also be impacted by the 2011 Grímsvötn eruption. As with the Mýrdalsjökull/Eyjafjallajökull ice variation time series following the Eyjafjallajökull eruption, we note that the 2011 melt season lags behind the average timing for Vatnajökull and that the seasonal mass loss is substantially less than average. The seasonal minimum for Vatnajökull in late-2011 is −0.48 m_{we} relative to an average of −0.75 m_{we}. The 2011 eruption resulted in a tephra layer predominantly to the south of the eruptive center with tephra thicknesses of 1–2 m within 7 km of the vent decreasing to thicknesses of 10 cm at 35 km [*Hreinsdóttir*, 2014]—thick enough to have had an insulating effect [*Nield et al.*, 2012; *Dragosics et al.*, 2016].

5. Discussion

5.1. Earth Model Elastic Parameters

For this work, we have chosen to use a half-space model tuned to fit our reduced data set. As stated previously, had we chosen instead to fit the original amplitudes, we would have chosen a half-space model with

Young's modulus of 45 GPa, ∼10% less than the Young's modulus value of our current preferred model. Both values are well within the range of Young's moduli of 30–130 GPa previously reported for half-space GIA modeling studies in Iceland [*Grapenthin et al.*, 2006; *Pinel et al.*, 2007; *Árnadóttir et al.*, 2009; *Auriac et al.*, 2013, 2014; *Zhao et al.*, 2014]. Although we tune our Earth model to fit the reduced data set (Figure 4), we find that the inversion results using the original and reduced data sets are not significantly different from each other for the 10 years from 2004 to 2014 (Figure 6), and the interpretations we draw from both inversion results are consistent. We again note that we use the amplitudes of seasonal motion to tune our Earth model, and we posit that at present, our inversion method depends less on the absolute magnitude of annual motion than on the pattern of spatial variability across the cGPS network—that is, the relative displacement between cGPS sites at any given epoch.

5.2. cGPS Corrections

We acknowledge an inconsistency introduced by correcting the cGPS time series as we have done for this work—that the ATML, CWS, and OBP displacements are computed using a different Earth model than that used for the rest of the analyses. Previous work evaluating ice cap-induced seasonal motion in Iceland did not consider ATML, CWS, or OBP loading [*Grapenthin et al.*, 2006; *Pinel et al.*, 2007] so we see our work as an incremental improvement. We also note that the environmental loading models used here to compute displacements are not accompanied by uncertainty estimates, so we do not propagate any errors associated with reducing the cGPS time series. Utilizing more detailed regional models of non-ice cap environmental loads or inverting for those loads simultaneously along with ice cap loading such as done by *Drouin et al.* [2016] may improve our results.

We do note, however, that correcting our cGPS time series for the effects non-ice environmental loads results in a change in the ratio of horizontal to vertical displacement amplitudes. The relationship between horizontal and vertical responses to loading is complex and, as noted by *Pinel et al.* [2007], such a ratio will change depending both on the Earth structure as well as distance from the load. If we are able to accurately estimate and remove non-ice cap related signals from the cGPS time series both in the vertical and horizontal components, future work may be able to use information about displacement ratios to better constrain a proper Earth model for Iceland.

5.3. Potential Implications for Volcanic Processes and Feedbacks

Tephra deposition following volcanic eruptions can have measureable impacts on glacial melt rates over many years. Reduction in surface albedo results as ash layers are incorporated into the ice caps and then reexposed during the summer melt season [*Möller et al.*, 2014] and as ash is resuspended and deposited onto ice during subsequent dust storms [*Arnalds et al.*, 2016]. *Möller et al.* [2014] found reduced surface albedo values for the tephra-influenced areas of Vatnajökull through the end of their study period in 2008 due to the Grímsvötn eruption in 2004. Conversely, localized insulation by tephra deposits may result in glacial advance [*Kirkbride and Dugmore*, 2003].

The effects of volcanism on ice melt rates can in turn impact volcanic processes themselves, thus creating the potential for process feedbacks between glacial melting and volcanism. Short-term surface load changes—such as an increased melting rate induced by changes in surface albedo—can perturb the stress conditions of shallow magma chambers and increase the likelihood of volcanic eruptions [*Albino et al.*, 2010]. For example, previous studies have demonstrated a seasonal pattern of the eruptive behavior of the Katla volcanic system in Iceland, noting that all eruptions during the last 400 years begin during times of surface ice melting in the spring to fall [*Larsen*, 2000; *Thordarson and Larsen*, 2007]. In addition, Katla eruptions have occurred at similar times as the three historical (last 1100 years) eruptions of Eyjafjallajökull prior to the 2010 eruption [*Sturkell et al.*, 2003; *Sigmundsson et al.*, 2010]. It follows, then, that the potential additive effects of reduced albedo due to tephra deposition following an Eyjafjallajökull eruption could enhance the seasonal changes in magma chamber stress conditions and increase the probability of Katla volcanic activity. Conversely, the 2010 Eyjafjallajökull eruption provides an example of the ways in which the relationship between the Katla and Eyjafjallajökull volcanic systems may be modulated by eruption size and tephra deposition thickness. Previously erupted volumes from the Eyjafjallajökull volcanic system have been small [e.g., *Sturkell et al.*, 2010] and may have acted to reduce albedo and increase melting of the Mýrdalsjökull/Eyjafjallajökull ice caps. However, the 2010 Eyjafjallajökull eruption produced a larger volume of ash relative to historic eruptions [*Gudmundsson et al.*, 2012; *Dragosics et al.*, 2016], which we have shown may have had an insulting effect on the Mýrdalsjökull/Eyjafjallajökull ice caps and could have
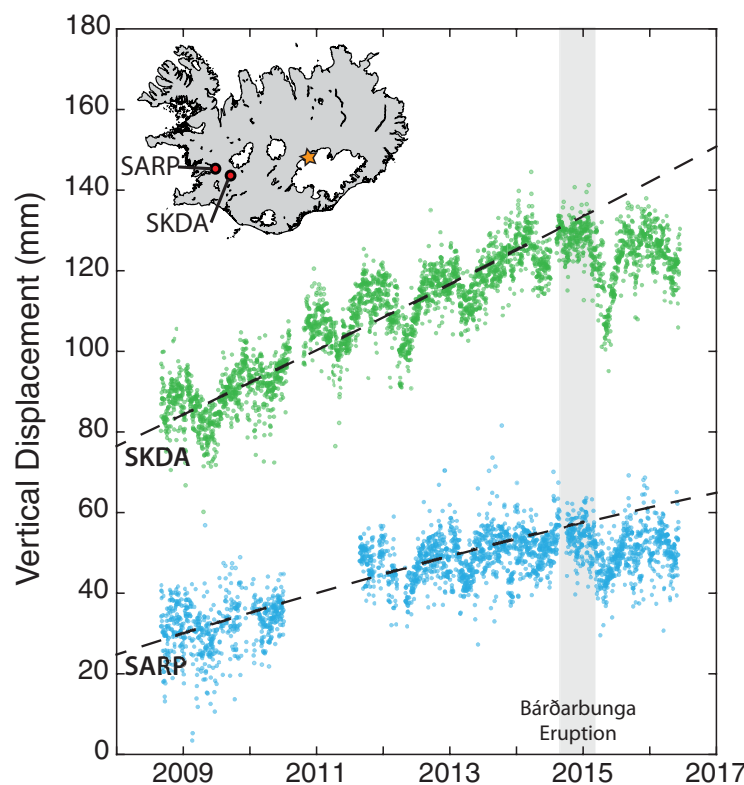
Figure 7. Post-2015 position estimates for some cGPS sites show subtle negative deviations relative to pre-2015 secular trends and accelerations (dashed lines), perhaps a response to Greenland meltwater accumulation in the North Atlantic and AMOC slow-down. If pervasive across Iceland, this signal is largely obscured by the effects of the Bárðarbunga eruption (timing and location of eruptive processes noted by shaded bar and orange star, respectively).

resulted in a reduction in Katla eruptive potential. Detecting the timing and magnitude of short-term surface load changes, as we have demonstrated here by inverting cGPS displacement time series, might improve our understanding of the changing pressure conditions of shallow magma chambers and the relationships between volcanic systems.

Future studies of the relationship between ice cap load variations and magma generation should include the potential feedback effects introduced by tephra deposition and changes in ice surface albedo. Many studies have demonstrated the link between deglaciation, surface uplift, and magma generation [e.g., *Jull and McKenzie*, 1996; *Pagli and Sigmundsson*, 2008; *Schmidt et al.*, 2013], however, no such study has yet included the potential effects of accelerated ice melt due to climate warming [*Compton et al.*, 2015] or the feedback processes introduced by volcanic tephra deposition.

5.4. Observing the Effects of Climate Change With cGPS

In Iceland, glaciers cover approximately 11% of the land surface and comprise the country's largest reservoir of freshwater [*Björnsson and Pálsson*, 2008]. Coupled climate-mass balance models predict dramatic losses in ice volume over the next two centuries [*Aðalgeirsdóttir et al.*, 2006, 2011], but regional changes may have contributed to recent localized mass gain. 2014/2015 mass balance measurements for Hofsjökull and Vatnajökull recorded mass gain for the first time in two decades [*Thorsteinsson*, 2015; *Foresta et al.*, 2016], perhaps a result of a negative sea surface temperature (SST) anomaly in the North Atlantic due to the accumulation of freshwater from Greenland melting and the slowing of the Atlantic meridional overturning circulation (AMOC) [*Rahmstorf*, 2015]. Although the cGPS record of Hofsjökull mass gain is largely obscured by the impacts of the concurrent Bárðarbunga eruption, some cGPS sites at sufficiently far distances from the eruptive center show subtle negative deviations from pre-2015 secular trends and accelerations (Figure 7). Continued cGPS monitoring of crustal responses to Iceland ice mass variation may provide important insights into the localized impacts of regional climate dynamics on seasonal time scales.

6. Conclusions

Mass variation time series derived from cGPS crustal motion observations present a low-cost complement to traditional mass balance measurements, and important contribution to the limited suite of tools currently available to quantify changes in ice cap mass on time scales shorter than 1 year. Through a simple least squares estimation scheme, we are able to produce Vatnajökull and Mýrdalsjökull/Eyjafjallajökull load variation time series that match the amplitudes representative of an average winter mass balance for each ice cap reported by *Grapenthin et al.* [2006] but that are not constrained to be perfectly periodic—thus better

representing the interannual variability recorded by field stake-based mass balance estimates [*Björnsson et al.*, 2013]. Although, as it exists now, the cGPS station density and network configuration results in load variation estimates for the Hofsjökull and Langjökull ice caps with errors of the same magnitude as their respective average annual winter balance, time series for the Vatnajökull and Mýrdalsjökull/Eyjafjallajökull ice caps allow for an examination of the timing and impact of seasonal snows, spring melting, and volcanic eruptions at a high temporal resolution.

With this new method, which, for the first time for Iceland incorporates information from the horizontal seasonal motion recorded by cGPS, we are able to resolve the annual and interannual variability of ice cap loading due to variations in precipitation and possibly also to changes in ice cap albedo and insulation due to tephra deposition following volcanic eruptions. This ability has implications for understanding short-term changes in the pressure conditions of shallow magma chambers, the potential feedbacks between volcanic activity and climate-driven ice loss, and volcanic hazards assessment. We expect that future campaigns to increase the spatial density of cGPS units in Iceland could result in the ability to use this or a similar inversion estimation scheme to monitor ice cap behavior in near real-time.

Appendix A

For this work, we have chosen to use an elastic half-space Earth model in order to maintain consistency with previous studies [*Grapenthin et al.*, 2006; *Pinel et al.*, 2007; *Árnadóttir et al.*, 2009; *Auriac et al.*, 2013, 2014; *Zhao et al.*, 2014]. Our goal above was to demonstrate the utility of inverting cGPS-measured crustal
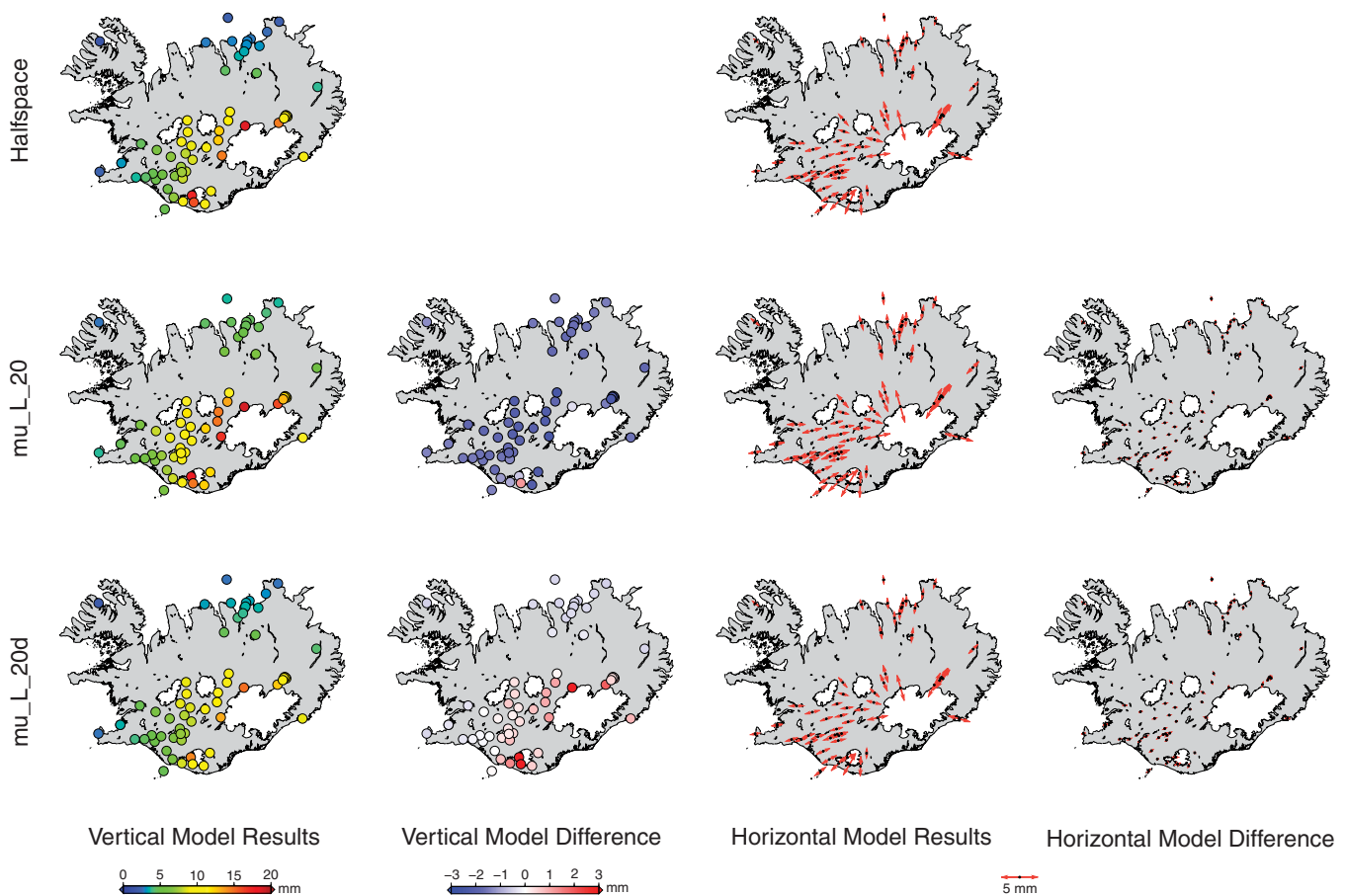

Figure A1. Comparing half-space and spherical Earth model-computed responses to loading by the average winter mass balances (Table 3). Half-space responses are the same as reported in Figure 4. Both spherical Earth models have been modified from the PREM Earth structure such that $\lambda = \mu = 20$ GPa to a depth of 1280 km. The model mu_L_20 maintains the PREM density structure while the model mu_L_20d has been modified to include a density of 2800 km/m³ to a depth of 1280 km. This density reduction is not compensated elsewhere in the model space and thus results in an inaccurate total Earth mass. Vertical motion RMSE values for the two spherical Earth models relative to the half-space model are 1.7 and 1.0 mm for models mu_L_20 and mu_L_20d, respectively.
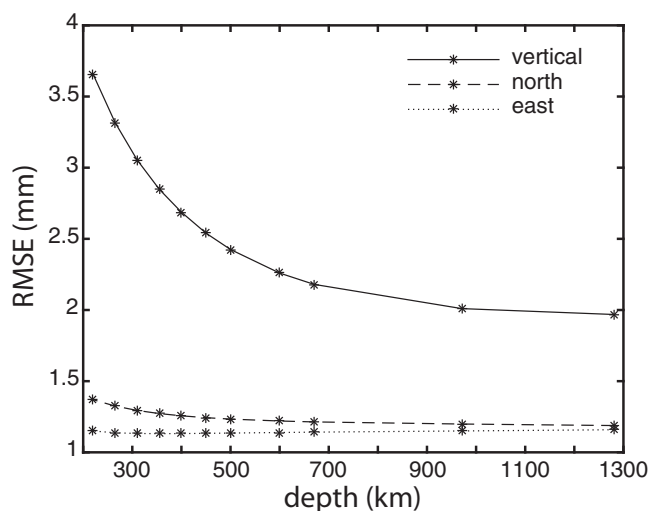
Figure A2. RMSE values of spherical Earth model-computed responses to loading by the average winter mass balances (Table 3) relative to the reduced (ATML, CWS, and OBP loading responses removed) cGPS seasonal displacement amplitudes. RMSE values decrease as the depth to the base of the modified layer increases—with limited improvement below ∼600 km. For these tests, a PREM spherical Earth model was modified such that that PREM density and Poisson's ratio were unchanged and only λ and μ were modified to give a constant Young's modulus value of 50 GPa.

motions to create meaningful load variation time series to compliment traditional mass balance measurements, but we note the value of cGPS-recorded seasonal amplitudes in determining a more detailed elastic structure of the Icelandic lithosphere and upper mantle. We share our preliminary test results using a spherical layered Earth model here as a demonstration.

In an attempt to fit our observations with a spherical layered Earth model, we computed displacements due to average winter loading (Table 3) over a 32 layer over fluid core PREM reference Earth model [*Dziewonski and Anderson*, 1981] using REAR [*Melini et al*., 2014] and found, as did *Drouin et al*. [2016], that the results required scaling of more than double to match amplitudes of seasonal motion—both reduced and original—observed by cGPS. We also found that two different scaling factors, one for vertical and one for horizontal, resulted in the best fit to our observations. Although this mismatch could, in part, be explained if the average winter loading values reported by *Grapenthin et al*. [2006] underestimate true seasonal loading amplitudes, such scaling suggests that the average PREM structure is clearly not capable of adequately describing the elastic properties of the lithosphere and mantle below Iceland.

We then attempted to fit our observations by adjusting the spherical layered Earth model parameters rather than simply scaling the PREM-computed values. In doing so, it is important to realize that the spatial distribution of the cGPS stations determines the sensitivity of the cGPS measurements to the internal structure of the Earth. Because of the limited size of Iceland, and the range of distances among the cGPS stations and the load centers (1–300 km), we expect that the cGPS measurements are sensitive only to the elastic properties of the upper mantle. We therefore ran a series of preliminary tests to investigate the effect of varying the elastic parameters of the upper mantle and lithosphere only. For each of these PREM modified models, we computed Love numbers up to degree 32,768 with the VE-CL0V3RS v3.5.3 (Visco-Elastic Compressible LOVe numbER Solver) and then computed the response with REAR [*Melini et al*., 2014].

In a first set of tests, we modified the PREM model by systematically reducing the values for the elastic parameters in the upper 200 km and including a 10 km thick low-velocity zone at either 10 or 40 km depth following receiver function studies that interpret a midcrustal low-velocity zone [*Darbyshire et al*., 2000] and Rayleigh wave inversions that find a low-velocity layer at the base of the crust [*Li and Detrick*, 2006]. Decreasing the elastic parameters and including low-velocity zones led to progressively larger displacement amplitudes, but even in the best fitting case, modeled displacements under-predicted observations by a factor of about 2.

However, the spatial pattern of the cGPS measurements (see, e.g., Figure 3) shows that the magnitude of seasonal vertical amplitudes decays slowly in the far field. In the context of the present model, this can only be explained if the departure from the PREM elastic properties extends deeper into the upper mantle. A variation in the lithosphere and in the mantle to a depth of 200 km would produce a signal that would be most prominent in the close proximity of the loads.

The poor performance of the spherical PREM-based model is puzzling, since at the spatial scale covered by the cGPS stations, the effect of the sphericity should be limited. Thus, we opted for a radical change in perspective. For this second set of tests, we modified a PREM spherical Earth model such that PREM density

and Poisson's ratio were unchanged and only λ and μ were modified to give a constant Young's modulus value of 50 GPa in an attempt to create a spherical model with elastic properties that matched that of the best fit half-space model. In this way, we created a suite of spherical Earth models that matched the elastic properties of the best fit half-space model down to a variety of depths. We found out that a spherical model with the same elastic properties (Young's modulus and Poisson's ratio) of the corresponding half-space model down to 1280 km, gives a fit to the data of quality comparable to the best half-space model (Figure A1). We also found, however, that variation of the Earth structure below 600 km depth results in diminishing data misfit reduction (Figure A2) confirming our speculation that the spatial distribution of cGPS stations results in limited depth-sensitivity.

These experiments are to be considered only as preliminary tests. Being able to reproduce the results of the half-space model with our significantly modified PREM-based models, allows us only to say that the PREM Earth structure is clearly not suitable to explain the elastic properties of the mantle below Iceland. Moreover, the models tested represent significant variations from the PREM elastic structure, and the resulting elastic parameterization would give, for example, seismic velocities inconsistent with those measured for Iceland [e.g., *Allen et al.*, 2002; *Li and Detrick*, 2006], both for the half-space and the spherical models. However, we think that these results are interesting and indicate that there is still a lot to be learned to explain the solid-Earth behavior of Iceland. Our preliminary results show that the cGPS network may be used as a tool to gain insight into the lithosphere and upper mantle of the Earth beneath Iceland. Combining cGPS measurements with other physical evidence to try to better constrain a spherical layered Earth model will be the subject of future studies.

References

Albino, F., V. Pinel, and F. Sigmundsson (2010), Influence of surface load variations on eruption likelihood: Application to two Icelandic sub-glacial volcanoes, Grímsvötn and Katla, *Geophys. J. Int.*, *181*, 1510–1524, doi:10.1111/j.1365-246X.2010.04603.x.

Allen, R. M., et al. (2002), Imaging the mantle beneath Iceland using integrated seismological techniques, *J. Geophys. Res.*, *107*(12), 2325, doi:10.1029/2001JB000595.

Altamimi, Z., X. Collilieux, and L. Métivier (2011), ITRF2008: An improved solution of the international terrestrial reference frame, *J. Geod.*, *85*(8), 457–473, doi:10.1007/s00190-011-0444-4.

Argus, D. F., Y. Fu, and F. W. Landerer (2014), Seasonal variation in total water storage in California inferred from GPS observations of vertical land motion, *Geophys. Res. Lett.*, *41*, 1971–1980, doi:10.1002/(ISSN)1944-8007.

Arnalds, O., P. Dagsson-Waldhauserova, and H. Olafsson (2016), The Icelandic volcanic aeolian environment: Processes and impacts—A review, *Aeolian Res.*, *20*, 176–195, doi:10.1016/j.aeolia.2016.01.004.

Auriac, A., K. H. Spaans, F. Sigmundsson, A. Hooper, P. Schmidt, and B. Lund (2013), Iceland rising: Solid Earth response to ice retreat inferred from satellite radar interferometry and visocelastic modeling, *J. Geophys. Res. Solid Earth*, *118*, 1331–1344, doi:10.1002/jgrb.50082.

Auriac, A., F. Sigmundsson, A. Hooper, K. H. Spaans, H. Björnsson, F. Pálsson, V. Pinel, and K. L. Feigl (2014), InSAR observations and models of crustal deformation due to a glacial surge in Iceland, *Geophys. J. Int.*, *198*(3), 1329–1341, doi:10.1093/gji/ggu205.

Aðalgeirsdóttir, G., T. Jóhannesson, H. Björnsson, F. Pálsson, and O. Sigurðsson (2006), Response of Hofsjökull and southern Vatnajökull, Iceland, to climate change, *J. Geophys. Res.*, *111*, F03001, doi:10.1029/2005JF000388.

Aðalgeirsdóttir, G., S. Guðmundsson, H. Björnsson, F. Pálsson, T. Jóhannesson, H. Hannesdóttir, S. P. Sigurðsson, and E. Berthier (2011), Modelling the 20th and 21st century evolution of Hoffellsjökull glacier, SE-Vatnajökull, Iceland, *Cryosphere*, *5*(4), 961–975, doi:10.5194/tc-5-961-2011.

Árnadóttir, T., B. Lund, W. Jiang, H. Geirsson, H. Björnsson, P. Einarsson, and T. Sigurdsson (2009), Glacial rebound and plate spreading: Results from the first countrywide GPS observations in Iceland, *Geophys. J. Int.*, *177*(2), 691–716, doi:10.1111/j.1365-246X.2008.04059.x.

Barbot, S. (2011), *Relax: Nonlinear Postseismic Relaxation in the Fourier Domain*: *User Manual*, Computational Infrastructure for Geodynamics, University of California, Davis, Calif. [Available at http://geodynamics.org/cig/software/relax/.]

Barbot, S., and Y. Fialko (2010), Fourier-domain Green's function for an elastic semi-infinite solid under gravity, with applications to earthquake and volcano deformation, *Geophys. J. Int.*, *182*(2), 568–582, doi:10.1111/j.1365-246X.2010.04655.x.

Björnsson, H., and F. Pálsson (2008), Icelandic glaciers, *Jökull*, *58*, 365–386.

Björnsson, H., F. Pálsson, S. Gudmundsson, E. Magnússon, G. Adalgeirsdóttir, T. Jóhannesson, E. Berthier, O. Sigurdsson, and T. Thorsteinsson (2013), Contribution of Icelandic ice caps to sea level rise: Trends and variability since the Little Ice Age, *Geophys. Res. Lett.*, *40*, 1546–1550, doi:10.1002/grl.50278.

Blewitt, G. (2003), Self-consistency in reference frames, geocenter definition, and surface loading of the solid Earth, *J. Geophys. Res.*, *108*(B2), 2103, doi:10.1029/2002JB002082.

Borsa, A. A., D. C. Agnew, and D. R. Cayan (2014), Ongoing drought-induced uplift in the western United States, *Science*, *345*(6204), 1587–1590, doi:10.1126/science.1260279.

Compton, K., R. A. Bennett, and S. Hreinsdottir (2015), Climate driven vertical acceleration of Icelandic crust measured by CGPS geodesy, *Geophys. Res. Lett.*, *42*, 743–750, doi:10.1002/(ISSN)1944-8007.

Darbyshire, F. A., K. F. Priestley, R. S. White, R. Stefánsson, G. B. Gudmundsson, and S. S. Jakobsdóttir (2000), Crustal structure of central and northern Iceland from analysis of teleseismic receiver functions, *Geophys. J. Int.*, *143*(1), 163–184, doi:10.1046/j.1365-246x.2000.00224.x.

Dong, D., T. Yunck, and M. Heflin (2003), Origin of the international terrestrial reference frame, *J. Geophys. Res.*, *108*(B4), 2200, doi:10.1029/2002JB002035.

Dragosics, M., O. Meinander, T. Jónsdóttír, T. Dürig, G. De Leeuw, F. Pálsson, P. Dagsson-Waldhauserova, and T. Thorsteinsson (2016), Insulation effects of Icelandic dust and volcanic ash on snow and ice, *Arabian J. Geosci.*, *9*(2), 126, doi:10.1007/s12517-015-2224-6.

Drouin, V., K. Heki, F. Sigmundsson, S. Hreinsdottir, and B. G. Ófeigsson (2016), Constraints on seasonal load variations and regional rigidity from continuous GPS measurements in Iceland, 1997–2014, *Geophys. J. Int.*, 205(3), 1843–1858, doi:10.1093/gji/ggw122.

Dziewonski, A. M., and D. L. Anderson (1981), Preliminary reference Earth model, *Phys. Earth Planet. Inter.*, 25, 297–356, doi:10.1016/0031-9201(81)90046-7.

Farrell, W. E. (1972), Deformation of the Earth by surface loads, *Rev. Geophys.*, 10(3), 761–797, doi:10.1029/RG010i003p00761.

Foresta, L., N. Gourmelen, F. Pálsson, P. Nienow, H. Björnsson, and A. Shepherd (2016), Surface elevation change and mass balance of Icelandic ice caps derived from swath mode CryoSat-2 altimetry, *Geophys. Res. Lett.*, 43, 12,138–12,145, doi:10.1002/2016GL071485.

Fu, Y., D. F. Argus, and F. W. Landerer (2015), GPS as an independent measurement to estimate terrestrial water storage variations in Washington and Oregon, *J. Geophys. Res. Solid Earth*, 120, 552–566, doi:10.1002/2014JB011415.

Fukumori, I. (2002), A partitioned Kalman filter and smoother, *Mon. Weather Rev.*, 130, 1370–1383, doi:10.1175/1520-0493(2002)130 < 1370: APKFAS>2.0.CO;2.

Geirsson, H., T. Árnadóttir, S. Hreinsdottir, J. Decriem, P. C. LaFemina, S. Jonsson, R. A. Bennett, S. Metzger, A. Holland, and E. Sturkell (2010), Overview of results from continuous GPS observations in Iceland from 1995 to 2010, *Jökull*, 60, 3–22.

Geirsson, H., et al. (2015), Geodetic observations of deep re-equilibration of magmatic systems accompanying the Hekla 2000 and Eyjafjallajökull 2010 eruptions, Iceland, *EGU Gen. Assem. Conf. Abstr.*, 17, 13344.

Grapenthin, R., F. Sigmundsson, H. Geirsson, T. Árnadóttir, and V. Pinel (2006), Icelandic rhythmics: Annual modulation of land elevation and plate spreading by snow load, *Geophys. Res. Lett.*, 33, L24305, doi:10.1029/2006GL028081.

Gudmundsson, S., H. Björnsson, E. Magnússon, E. Berthier, F. Pálsson, M. T. Gudmundsson, T. Högnadóttir, and J. Dall (2011), Response of Eyjafjallajökull, Torfajökull and Tindfjallajökull ice caps in Iceland to regional warming, deduced by remote sensing, *Polar Res.*, 30, Article 7282, doi:10.1016/S0264-3707(02)00042-X.

Gudmundsson, M. T., et al. (2012), Ash generation and distribution from the April-May 2010 eruption of Eyjafjallajökull, Iceland, *Sci. Rep.*, 2, Article 572, doi:10.1038/srep00572.

Herring, T. A., R. W. King, and S. C. McClusky (2010a), *GAMIT Reference Manual: GPS Analysis at MIT, Release 10.4*, Mass. Inst. of Technol., Cambridge.

Herring, T. A., R. W. King, and S. C. McClusky (2010b), *GLOBK Reference Manual: Global Kalman Filter VLBI and GPS Analysis Program, Release 10.4*, Mass. Inst. of Technol., Cambridge.

Hock, R., M. de Woul, V. Radić, and M. Dyurgerov (2009), Mountain glaciers and ice caps around Antarctica make a large sea-level rise contribution, *Geophys. Res. Lett.*, 36, L07501, doi:10.1029/2008GL037020.

Hreinsdóttir, S., T. Árnadóttir, J. Decriem, H. Geirsson, A. Tryggvason, R. A. Bennett, and P. LaFemina (2009), A complex earthquake sequence captured by the continuous GPS network in SW Iceland, *Geophys. Res. Lett.*, 36, L12309, doi:10.1029/2009GL038391.

Hreinsdóttir, S., et al. (2014), Volcanic plume height correlated with magma-pressure change at Grímsvötn Volcano, Iceland, *Nat. Geosci.*, 7(3), 214–218, doi:10.1038/ngeo2044.

Iceland Meteorological Office (2010), The weather in Iceland 2009, Reykjavik, Iceland. [Available at http://en.vedur.is/weather/articles/nr/1802.]

Jacob, T., J. Wahr, W. T. Pfeffer, and S. Swenson (2012), Recent contributions of glaciers and ice caps to sea level rise, *Nature*, 482(7386), 514–518, doi:10.1038/nature10847.

Jóhannesson, T., H. Björnsson, E. Magnússon, S. Guðmundsson, F. Pálsson, O. Sigurðsson, T. Thorsteinsson, and E. Berthier (2013), Ice-volume changes, bias estimation of mass-balance measurements and changes in subglacial lakes derived by lidar mapping of the surface of Icelandic glaciers, *Ann. Glaciol.*, 54(63), 63–74, doi:10.3189/2012AoG63A422.

Jónsdóttir, J. F. (2010), A runoff map based on numerically simulated precipitation and a projection of future runoff in Iceland/Une carte d'écoulement basée sur la précipitation numériquement simulée et un scénario du futur écoulement en Islande, *Hydrol. Sci. J.*, 53(1), 100–111, doi:10.1623/hysj.53.1.100.

Jull, M., and D. McKenzie (1996), The effect of deglaciation on mantle melting beneath Iceland, *J. Geophys. Res.*, 101(B10), 21,815–21,828, doi:10.1029/96JB01308.

Kalnay, E., et al. (1996), The NCEP/NCAR 40-year reanalysis project, *Bull. Am. Meteorol. Soc.*, 77, 437–470, doi:10.1175/1520-0477(1996)077<0437: TNYRP>2.0.CO;2.

Kirkbride, M. P., and A. J. Dugmore (2003), Glaciological response to distal tephra fallout from the 1947 eruption of Hekla, south Iceland, *J. Glaciol.*, 49(166), 420–428, doi:10.3189/172756503781830575.

Larsen, G. (2000), Holocene eruptions within the Katla volcanic system, south Iceland: Characteristics and environmental impact, *Jökull*, 49, 1–28.

Li, A., and R. S. Detrick (2006), Seismic structure of Iceland from Rayleigh wave inversions and geodynamic implications, *Earth Planet. Sci. Lett.*, 241(3–4), 901–912, doi:10.1016/j.epsl.2005.10.031.

Lyard, F., F. Lefevre, T. Letellier, and O. Francis (2006), Modelling the global ocean tides: Modern insights from FES2004, *Ocean Dyn.*, 56(5–6), 394–415, doi:10.1007/s10236-006-0086-x.

Magnússon, E., H. Björnsson, J. Dall, and F. Pálsson (2005), The 20th century retreat of ice caps in Iceland derived from airborne SAR: W-Vatnajökull and N-Mýrdalsjökull, *Earth Planet. Sci. Lett.*, 237(3–4), 508–515, doi:10.1016/j.epsl.2005.06.038.

Melini, D., P. Gegout, G. Spada, and M. A. King (2014), *REAR—A Regional ElAstic Rebound Calculator, User Manual for Version 1.0*. [Available at http://hpc.rm.ingv.it/rear.]

Möller, R., M. Möller, H. Björnsson, S. Guðmundsson, F. Pálsson, B. Oddsson, P. A. Kukla, and C. Schneider (2014), MODIS-derived albedo changes of Vatnajökull (Iceland) due to tephra deposition from the 2004 Grímsvötn eruption, *Int. J. Appl. Earth Obs. Geoinf.*, 26, 256–269, doi:10.1016/j.jag.2013.08.005.

Möller, R., M. Möller, P. Kukla, and C. Schneider (2016), Impact of supraglacial deposits of tephra from Grímsvötn volcano, Iceland, on glacier ablation, *J. Glaciol.*, 62(235), 933–943, doi:10.1017/jog.2016.82.

Nield, J. M., R. C. Chiverrell, S. E. Darby, J. Leyland, L. H. Vircavs, and B. Jacobs (2012), Complex spatial feedbacks of tephra redistribution, ice melt and surface roughness modulate ablation on tephra covered glaciers, *Earth Surf. Processes Landforms*, 38(1), 95–102, doi:10.1002/esp.3352.

Ouellette, K. J., C. de Linage, and J. S. Famiglietti (2013), Estimating snow water equivalent from GPS vertical site-position observations in the western United States, *Water Resour. Res.*, 49, 2508–2518, doi:10.1002/wrcr.20173.

Pagli, C., and F. Sigmundsson (2008), Will present day glacier retreat increase volcanic activity? Stress induced by recent glacier retreat and its effect on magmatism at the Vatnajökull ice cap, Iceland, *Geophys. Res. Lett.*, 35, L09304, doi:10.1029/2008GL033510.

Pinel, V., F. Sigmundsson, E. Sturkell, H. Geirsson, P. Einarsson, M. T. Gudmundsson, and T. Högnadóttir (2007), Discriminating volcano deformation due to magma movements and variable surface loads: Application to Katla subglacial volcano, Iceland, *Geophys. J. Int.*, 169(1), 325–338, doi:10.1111/j.1365-246X.2006.03267.x.

Rahmstorf, S., J. E. Box, G. Feulner, M. E. Mann, A. Robinson, S. Rutherford, and E. J. Schaffernicht, (2015) Exceptional twentieth-century slowdown in Atlantic Ocean overturning circulation, *Nat. Clim. Change*, 5(5), 475–480, doi:10.1038/nclimate2554.

Rodell, M., et al. (2004), The global land data assimilation system, *Bull. Am. Meteorol. Soc.*, *85*(3), 381–394, doi:10.1175/BAMS-85-3-381.

Rui, H. (2011), Readme document for global land data assimilation system, Version 1 (GLDAS-1), Goddard Earth Sciences Data and Information Services Center (GES DISC), Greenbelt, Md. [Available at http://disc.sci.gsfc.nasa.gov/services/grads-gds/gldas.]

Schmidt, P., B. Lund, C. Hieronymus, J. Maclennan, T. Árnadóttir, and C. Pagli (2013), Effects of present-day deglaciation in Iceland on mantle melt production rates, *J. Geophys. Res. Solid Earth*, *118*, 3366–3379, doi:10.1002/jgrb.50273.

Sigmundsson, F., et al. (2010), Intrusion triggering of the 2010 Eyjafjallajökull explosive eruption, *Nature*, *468*(7322), 426–430, doi:10.1038/nature09558.

Sigmundsson, F., et al. (2014), Segmented lateral dyke growth in a rifting event at Barðarbunga volcanic system, Iceland, *Nature*, *517*(7533), 191–195, doi:10.1038/nature14111.

Sørensen, L. S., A. H. Jarosch, G. Aðalgeirsdóttir, V. R. Barletta, R. Forsberg, F. Pálsson, H. Björnsson, and T. Jóhannesson (2017), The effect of signal leakage and glacial isostatic rebound on GRACE-derived ice mass changes in Iceland, *Geophys. J. Int.*, *209*, 226–233, doi:10.1093/gji/ggx008.

Sturkell, E., F. Sigmundsson, and P. Einarsson (2003), Recent unrest and magma movements at Eyjafjallajökull and Katla volcanoes, Iceland, *J. Geophys. Res.*, *108*(B8), 2369, doi:10.1029/2001JB000917.

Sturkell, E., P. Einarsson, F. Sigmundsson, A. Hooper, B. G. Ófeigsson, H. Geirsson, and H. Ólafsson (2010), Katla and Eyjafjallajökull volcanoes, *Dev. Quat. Sci.*, *13*, 5–21, doi:10.1016/S1571-0866(09)01302-5.

Tapley, B. D., S. Bettadpur, M. Watkins, and C. Reigber (2004), The gravity recovery and climate experiment: Mission overview and early results, *Geophys. Res. Lett.*, *31*, L09607, doi:10.1029/2004GL019920.

Thordarson, T., and G. Larsen (2007), Volcanism in Iceland in historical time: Volcano types, eruption styles and eruptive history, *J. Geodyn.*, *43*(1), 118–152, doi:10.1016/j.jog.2006.09.005.

Thorsteinsson, T. (2015), Hofsjökull ice cap gains mass: For the first time in twenty years the Hofsjökull ice cap gains mass, Iceland Meteorol. Off., Reykjavik, Iceland. [Available at http://en.vedur.is/about-imo/news/nr/3229.]

Van Dam, T. M., and J. M. Wahr (1987), Displacements of the Earth's surface due to atmospheric loading: Effects on gravity and baseline measurements, *J. Geophys. Res.*, *92*(B2), 1281–1286, doi:10.1029/JB092iB02p01281.

Wouters, B., D. Chambers, and E. J. O. Schrama (2008), GRACE observes small-scale mass loss in Greenland, *Geophys. Res. Lett.*, *35*, L20501, doi:10.1029/2008GL034816.

Zhao, W., F. Amelung, T. H. Dixon, S. Wdowinski, and R. Malservisi (2014), A method for estimating ice mass loss from relative InSAR observations: Application to the Vatnajökull ice cap, Iceland, *Geochem. Geophys. Geosyst.*, *15*, 108–120, doi:10.1002/2013GC004936.